Earth System
Dynamics

The implications of maintaining Earth's hemispheric albedo symmetry for shortwave radiative feedbacks

Aiden R. Jönsson[1,2] **and Frida A.-M. Bender**[1,2]

[1]Department of Meteorology, Stockholm University, 106 91 Stockholm, Sweden
[2]Bolin Centre for Climate Research, Stockholm University, 106 91 Stockholm, Sweden

Correspondence: Aiden R. Jönsson (aiden.jonsson@misu.su.se)

Abstract. The Earth's albedo is observed to be symmetric between the hemispheres on the annual mean timescale, despite the clear-sky albedo being asymmetrically higher in the Northern Hemisphere due to more land area and aerosol sources; this is because the mean cloud distribution currently compensates for the clear-sky asymmetry almost exactly. We investigate the evolution of the hemispheric difference in albedo in the Coupled Model Intercomparison Project Phase 6 (CMIP6) coupled model simulations following an abrupt quadrupling of CO_2 concentrations, to which all models respond with an initial decrease of albedo in the Northern Hemisphere (NH) due to loss of Arctic sea ice. Models disagree over whether the net effect of NH cloud responses is to reduce or amplify initial NH albedo reductions. After the initial response, the evolution of the hemispheric albedo difference diverges among models, with some models remaining stably at their new hemispheric albedo difference and others returning towards their pre-industrial difference primarily through a reduction in SH cloud cover. Whereas local increases in cloud cover contribute to negative shortwave cloud feedback, the cross-hemispheric communicating mechanism found to be primarily responsible for restoring hemispheric symmetry in the models studied implies positive shortwave cloud feedback.

1 Introduction

The Earth's albedo is hemispherically symmetric to a high degree; the Northern Hemisphere (NH) minus Southern Hemisphere (SH) difference in annual mean hemispheric albedo (henceforth referred to as asymmetry) has been on the order of $0.1\,\mathrm{W\,m^{-2}}$ for the past 2 decades (Datseris and Stevens, 2021; Jönsson and Bender, 2022). This was first noted, although with greater uncertainty, during the first generation of satellite observations of Earth's radiative energy balance (Vonder Haar and Suomi, 1971) and persists without detectable trends in modern satellite observations (Stevens and Schwartz, 2012; Voigt et al., 2013; Stephens et al., 2015; Datseris and Stevens, 2021; Jönsson and Bender, 2022). This is possible because, in the annual mean all-sky albedo, clouds compensate for the clear-sky albedo asymmetry that exists due to differences in surface properties and aerosol loading between the NH and SH (Stephens et al., 2015; Jönsson and Bender, 2022; Diamond et al., 2022). Climate models have

a large spread of albedo asymmetry (Stephens et al., 2015; Jönsson and Bender, 2022), but the variability of asymmetry in model simulations is low, with most coupled models exhibiting relatively small changes between pre-industrial (PI) and present-day (PD) historical asymmetries (Jönsson and Bender, 2022).

The clear-sky hemispheric albedo asymmetry is determined mostly by contributions from the clear-sky atmosphere (Stephens et al., 2015; Jönsson and Bender, 2022), pointing to a strong influence of aerosols in the NH in leading to a presently higher NH than SH clear-sky albedo (Diamond et al., 2022). In higher latitudes, the surface contributes a greater share of the albedo (Stephens et al., 2015). Because of aerosol emission drawdown and changes in the cryosphere due to global warming, the clear-sky hemispheric albedo asymmetry is likely to change in the near future (Diamond et al., 2022).

Higher cloud amount in the SH subtropics and higher cloud amount and cloud albedo in the SH midlatitudes compared to their NH counterparts compensate for both the clearsky albedo asymmetry and the higher cloud amount in the NH tropics compared to in the SH tropics (Bender et al., 2017). Although it has been shown that the tropical maximum in deep convective cloud cover following the position of the Intertropical Convergence Zone (ITCZ) could offer some compensation to a hemispheric difference in albedo by shifting into the darker, warmer hemisphere (Voigt et al., 2013, 2014), tropical clouds have been understood not to have a major role in determining the hemispheric albedo symmetry, since the tropical maximum in cloud cover is located in the NH. Thus, extratropical cloud cover – particularly in the SH midlatitudes – has been highlighted as important for maintaining the hemispheric albedo symmetry in the annual mean and beyond (Datseris and Stevens, 2021; Jönsson and Bender, 2022; Rugenstein and Hakuba, 2023), while variability in tropical cloud cover has been found to contribute to variability in the albedo asymmetry time series (Jönsson and Bender, 2022). Changes in SH extratropical clouds in response to anthropogenic forcing would inevitably impact the hemispheric albedo symmetry; furthermore, clouds in the SH extratropics are responsible for a large share of the positive shift in model estimates of shortwave (SW) cloud feedbacks from CMIP5 to CMIP6 (Zelinka et al., 2020). However, constraining the magnitude of this shift and the representation of SH extratropical clouds in models is made challenging due to a lack of observations (Ceppi and Hartmann, 2015; Gettelman et al., 2020).

The Earth's albedo is to a large degree determined by contributions from clouds, accounting for over half of the upwelling shortwave (SW) radiative fluxes at the top of the atmosphere (TOA) in the global mean. This means that the planetary albedo is relatively sensitive to changes in cloud properties and coverage with a changing climate. The sum effect of clouds on changes in planetary albedo and thus reflected SW radiation on Earth's radiative balance at the TOA in response to change in temperature is referred to as the total SW cloud radiative feedback, and its spatial distribution, as well as its global mean magnitude, is the greatest source of uncertainty in estimating the climate's sensitivity to CO_2 forcing (Forster et al., 2021). The spread of SW cloud radiative feedbacks estimated by coupled models has increased in the latest phase of the Coupled Model Intercomparison Project (CMIP6) compared to in the previous CMIP5, and its average value has increased from slightly negative in CMIP5 to slightly positive in CMIP6 (Zelinka et al., 2020). Observational constraints also support this positive SW cloud radiative feedback estimate (Ceppi and Nowack, 2021; Forster et al., 2021). The hemispheric albedo symmetry is thereby relevant in addressing a significant source of uncertainty in constraining estimates of climate sensitivity: understanding any mechanisms that might maintain this symmetry can aid

in estimating the magnitude and distribution of the total SW cloud radiative feedback.

While there is no known physical mechanism or explanation for the observed hemispheric albedo symmetry, it is important to pose the following question: what would a mechanism for maintaining a hemispheric albedo symmetry entail for climate? Given that there is no observed trend in the hemispheric difference in albedo despite changes in the global radiative energy balance and despite global changes in albedo (Stephens et al., 2022), the hemispheric symmetry is at least robust throughout the satellite record. In this study, we investigate the implications for Earth's climate if its albedo were forced out of its current hemispheric symmetry due to warming processes to guide an exploration of possibilities for changes in the global cloud distribution in a changing climate.

We examine possible pathways for the Earth's albedo symmetry response to warming using climate models, and we discuss how these pathways for hemispheric albedo differences in a perturbed climate manifest in terms of changes to the cloud distribution, heat transport, energy balance, and warming. To this end, we use simulations from an ensemble of coupled atmosphere–ocean and Earth system models from the Coupled Model Intercomparison Project Phase 6 (CMIP6) (Eyring et al., 2016) in which CO_2 concentrations are abruptly quadrupled from PI levels. These idealized single-forcing experiments allow for the study of the evolution of albedo asymmetry in models in response only to greenhouse gas (GHG)-forced warming, without consideration of aerosol forcing that is presently significant but can be expected to be much smaller than the CO_2 forcing in the future if ongoing aerosol emission drawdown continues (Myhre et al., 2015; Szopa et al., 2021). We show how modeled albedo asymmetries evolve as the climate warms, and we categorize model behavior by symmetry-maintaining responses (Sect. 3.1). We then characterize potential albedo-symmetry-maintaining mechanisms and how strongly they act among the models (Sect. 3.2 and 3.3). Finally, we describe the implications that symmetry-maintaining mechanisms have for the strength of SW cloud radiative feedbacks (Sect. 3.4) and discuss the realism of these mechanisms (Sect. 4).

2 Materials and methods

2.1 Model output

In this analysis, we use CMIP6 abrupt, strong forcing (*abrupt-4xCO2*) experiments, as well as simulations of PI conditions (*piControl*) and those using best estimates of past forcings (*historical*) (Eyring et al., 2016). Abrupt forcing simulations can be used to estimate a model's equilibrium climate sensitivity (ECS) by regressing its global mean temperature response against its net TOA radiation imbalance; this slope yields the effective climate sensitivity (EffCS),

a first-order estimate of ECS (Gregory et al., 2004). This method requires a reasonable amount of simulation time (the minimum for CMIP6 participation being 150 years) compared to the millennia that are needed for a model's climate to equilibrate and yield a calculation of the ECS (Rugenstein et al., 2020) and thus includes a high number of models. The abrupt forcing simulations allow sequences of events in the adjustment of the climate system to be studied as they occur on different timescales. In this study, from 34 models (listed in Table 1), we consider one realization from each ($r1i1p1f1$) and discuss their evolution over 150 years of simulation time following the onset of forcing. We use one realization ($r1i1p1f1$) of historical simulations for each model to estimate values of PD conditions over the years 2000–2014 to compare to the Clouds and the Earth's Radiant Energy System Energy Balanced and Filled (CERES EBAF) radiative fluxes and the Moderate Resolution Imaging Spectroradiometer (MODIS) cloud fraction obtained from observations over March 2000–February 2015 (Loeb et al., 2018). We also make use of estimates of model radiative feedback strengths published by Zelinka et al. (2022) and model ECS published by Meehl et al. (2020). We choose only models where all radiative flux variables were available. Certain models are excluded when output needed for a given comparison was not available; variable output coverage is specified in Appendix A.

2.2 Data processing

We focus our analysis on modeled reflected SW radiative fluxes at the TOA ($F_{\text{TOA}}^{\uparrow}$) and albedo α in all- and clear-sky conditions, as well as the SW cloud radiative effect (CRE), defined as the difference between clear- and all-sky $F_{\text{TOA}}^{\uparrow}$:

$$\text{SW CRE} = F_{\text{TOA, clear}}^{\uparrow} - F_{\text{TOA, all}}^{\uparrow}, \tag{1}$$

so that a negative CRE implies TOA cooling. NH minus SH hemispheric differences in $F_{\text{TOA}}^{\uparrow}$ are referred to as *asymmetry*, and hemispheric differences in other values are denoted with δ_{HD}. Differences in time are denoted with Δ. Area averages are calculated using meridional weights given by the cosine of latitude, i.e., assuming a spherical Earth model. In calculating time averages, we weight CERES EBAF time averages by the length of months in days, but we do not weight monthly averages in models by the length of the month due to differences in model calendars; we motivate this with the assumption that differences in time averages among the 34 models presented here should arise primarily from differences in the models themselves and secondarily by the 5 d ($\sim 1\%$) spread in model calendar years. Where correlation statistics are given, the correlation is significant at the 99 % confidence level ($p < 0.01$) unless otherwise stated.

To estimate meridional heat transport (MHT) and its components, we use monthly mean TOA and surface energy fluxes following the methods outlined in Donohoe et al. (2020). We show only the tendency of meridional redistributions of energy absorbed by the climate system, as the modeled climate systems in these simulations are not in equilibrium. The implied total (ocean plus atmosphere) MHT is assumed to be driven by the meridional distribution of TOA energy imbalance, and the implied atmospheric heat transport (AHT) is assumed to be driven by the energy input into the atmosphere or the difference between the TOA energy input and the total surface energy input.

3 Results

3.1 Modeled albedo asymmetry responses to CO_2 forcing

Figure 1 depicts the time evolution of modeled asymmetries relative to their PI mean hemispheric albedo difference. In all models, asymmetry immediately becomes more negative following a reduction of clear-sky albedo asymmetry, which occurs primarily in the first 50 years after the forcing is applied; from here on, we will refer to the period between 30–50 years into the experiment as Mid, and we will use its mean conditions as being representative of the model state after the initial albedo asymmetry response. After the Mid period, the evolution of the asymmetry time series diverges among the models, with some models' asymmetry remaining relatively stable and others recovering towards their PI mean asymmetry; this divergence is driven by cloud responses. We will henceforth refer to the years 130–150 as the End period. The divergence of asymmetry responses after Mid can be seen in the distribution of asymmetry differences between End and Mid (Fig. 1c). The correlation between clear- and all-sky asymmetry responses between Mid and PI conditions is strong ($R^2 = 0.78$) and weak between the End and Mid periods ($R^2 = 0.33$), illustrating the role of clouds in the divergence of asymmetry responses following the initial response. In two models, EC-Earth3-Veg and EC-Earth3-AerChem, asymmetry continues to strengthen in the negative direction due to continued NH darkening. By 150 years, several models have recovered their PI mean asymmetry, with some overcompensating towards a more positive asymmetry than in PI conditions.

By End, modeled responses in hemispheric differences in net TOA energy inputs are also anticorrelated with asymmetry responses ($R^2 = 0.79$, 0.41, and 0.39 for all-sky, clear-sky, and CRE asymmetry responses, respectively), with a change of $-0.92\,\text{W m}^{-2}$ for each W m^{-2} difference in the all-sky asymmetry response. A positive disturbance in the NH–SH hemispheric mean difference in net TOA energy input would induce anomalous southward cross-equatorial heat transport – or, if cross-equatorial transport is not changed, hemispherically asymmetric warming and/or deep-ocean heat storage.

Figure 2 includes profiles of zonal mean changes in all- and clear-sky reflected radiation, as well as SW CRE

Table 1. CMIP6 member models used in this study and their representative numbers when model number is displayed in figures.

	Model	Citation (abrupt-4xCO2, piControl, historical)
(1)	ACCESS-CM2	Dix et al. (2019a, b, c)
(2)	AWI-CM-1-1-MR	Semmler et al. (2018a, c, b)
(3)	BCC-CSM2-MR	Wu et al. (2018a, c, b)
(4)	BCC-ESM1	Zhang et al. (2019b, 2018b, a)
(5)	CAMS-CSM1-0	Rong (2019a, c, b)
(6)	CESM2	Danabasoglu (2019a); Danabasoglu et al. (2019); Danabasoglu (2019d)
(7)	CESM2-FV2	Danabasoglu (2020a, 2019g, c)
(8)	CESM2-WACCM	Danabasoglu (2019b, h, f)
(9)	CESM2-WACCM-FV2	Danabasoglu (2020b, 2019i, e)
(10)	CMCC-CM2-SR5	Lovato and Peano (2020a, c, b)
(11)	CanESM5	Swart et al. (2019a, b, c)
(12)	EC-Earth3-AerChem	EC-Earth Consortium (2020a, c, b)
(13)	EC-Earth3-Veg	EC-Earth Consortium (2019a, c, b)
(14)	FGOALS-f3-L	Yu (2019a, c, b)
(15)	FGOALS-g3	Li (2019a, c, b)
(16)	GFDL-CM4	Guo et al. (2018a, b, c)
(17)	GFDL-ESM4	Krasting et al. (2018a, b, c)
(18)	GISS-E2-1-G	NASA Goddard Institute for Space Studies (2018a, c, b)
(19)	GISS-E2-1-H	NASA Goddard Institute for Space Studies (2019a, 2018d, 2019b)
(20)	GISS-E2-2-G	NASA Goddard Institute for Space Studies (2019c, d)
(21)	IITM-ESM	Gopinathan et al. (2019); Narayanasetti et al. (2019); Choudhury et al. (2019)
(22)	INM-CM4-8	Volodin et al. (2019a, c, b)
(23)	INM-CM5-0	Volodin et al. (2019d, f, e)
(24)	IPSL-CM6A-LR	Boucher et al. (2018a, c, b)
(25)	KACE-1-0-G	Byun et al. (2019a, c, b)
(26)	MIROC6	Tatebe and Watanabe (2018a, c, b)
(27)	MPI-ESM-1-2-HAM	Neubauer et al. (2019a, b, c)
(28)	MPI-ESM1-2-HR	Jungclaus et al. (2019a, b, c)
(29)	MPI-ESM1-2-LR	Wieners et al. (2019a, b, c)
(30)	MRI-ESM2-0	Yukimoto et al. (2019b, c, a)
(31)	NESM3	Cao and Wang (2019a, c, b)
(32)	NorESM2-MM	Bentsen et al. (2019a, b, c)
(33)	SAM0-UNICON	Park and Shin (2019a, c, b)
(34)	TaiESM1	Lee and Liang (2020a, c, b)

throughout the simulations; composite maps and maps of inter-model spread for these variables are shown in Figs. S1–S3 in the Supplement. Figure 2 shows that the initial negative asymmetry response is due primarily to a reduction in NH high-latitude clear-sky albedo (Fig. 2a) and secondarily to changes in NH cloud cover (Fig. 2b). Polar albedo reductions in the SH are generally smaller than those in the NH. High-latitude NH albedo losses are consistent with other studies on the amplified warming of the Arctic in response to GHG forcing (e.g., Hahn et al., 2021; Sledd and L'Ecuyer, 2021) and can be ascribed to sea ice loss. While models agree on the direction of SW CRE changes in the Arctic, they disagree on the direction of SW CRE changes at other latitudes in the NH (Fig. 2c, f); the NH albedo responses will be discussed in Sect. 3.2. Models that recover towards their PI mean asymmetry by the end of the simulation do so primarily by weakening negative SH midlatitude SW CRE beyond Mid (Fig. 2i); these responses will be discussed in Sect. 3.3. All

models generally see a weakening in subtropical SW CRE in both hemispheres throughout the 150 years.

It is important to note that we present the evolution of modeled albedo asymmetry relative to PI conditions to study its potential response to warming, and there is a large spread in PI mean hemispheric albedo differences among models (Fig. 1c; Jönsson and Bender, 2022; Diamond et al., 2022; Rugenstein and Hakuba, 2023). However, we do not see any consistent or robust dependence of the asymmetry response upon PI mean asymmetries across models, which is in agreement with Rugenstein and Hakuba (2023).

3.2 Initial NH cloud compensations to clear-sky darkening

Although the asymmetry response following the initial NH surface darkening is unanimous among models in terms of sign, there is spread in the magnitude of this asymme-
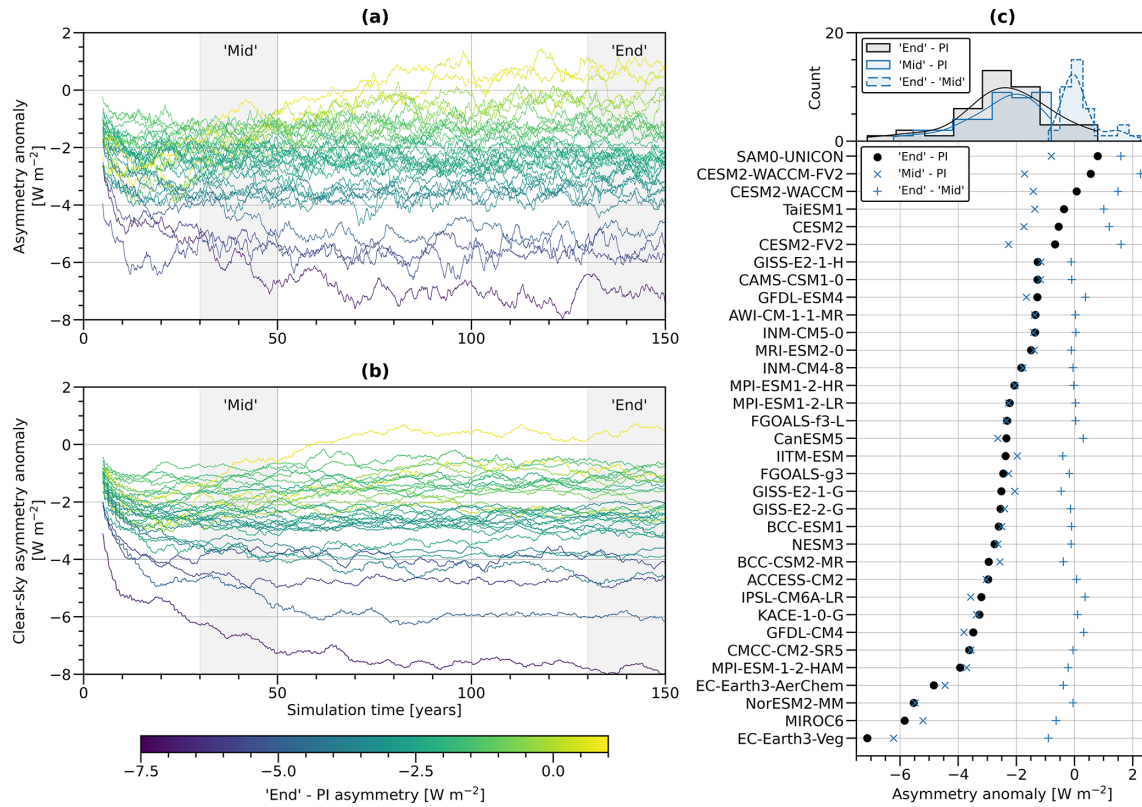
Figure 1. (a, b) Time series of 5-year running mean modeled **(a)** all-sky and **(b)** clear-sky asymmetry responses in abrupt-4xCO2 simulations. The color scale of time series lines is representative of the total End minus PI albedo asymmetry difference. **(c)** Differences in mean asymmetries between periods, listed in order of End minus PI asymmetry changes. Histograms (with eight bins; also shown as curves smoothed with a Gaussian kernel) of the distributions of asymmetry responses by period are shown at the top.

try response. Models disagree on whether cloud responses strengthen or dampen the NH clear-sky albedo reduction seen in the asymmetry time series. Disturbances in the hemispheric albedo symmetry with warming may be reduced by clouds when they buffer clear-sky albedo reductions; we will refer to these compensations as *local compensations*, and we will present modeled NH cloud responses in order to interpret the degree of local compensations in the hemisphere where clear-sky albedo reductions are greatest. To understand where clouds and clear-sky albedo changes are impacting the initial NH darkening the most, changes in the clear- and all-sky reflected SW radiation, as well as SW CRE, in three ranges of latitudes are presented in Fig. 3. Figure 2 shows that most of these responses in the NH occur primarily by the end of the Mid period and evolve less thereafter; changes after Mid occur mostly in high latitudes.

Poleward of 60° N, models agree that clouds reduce the impact of the loss of Arctic ice cover on Arctic planetary albedo, as has been detailed in Sledd and L'Ecuyer (2021), although they disagree on the magnitude of this cloud compensation for surface albedo darkening. However, the overall impact of clouds on NH albedo varies between models despite masking the surface albedo reduction in higher lati-

tudes. The response in Arctic SW CRE has only a weak bearing on the overall change in NH SW CRE ($R^2 = 0.15$ with $p = 0.02$) and virtually none on the total NH albedo change ($R^2 < 0.01$ with $p = 0.95$) between PI conditions and Mid.

By Mid, SW CRE is weakened among all models to varying degrees in the NH subtropics to midlatitudes, leading to a reduction in albedo. However, models disagree over whether clouds in the NH tropics amplify or compensate for the reduction in albedo. In some models, changes in tropical cloud cover cause SW CRE to strengthen and increase albedo; these models have a weaker overall reduction in NH albedo and thus weaker initial albedo asymmetry response.

The sum effect of these changes is that models disagree on whether clouds would amplify or reduce the initial NH albedo decrease caused by changes in clear-sky albedo during warming, depending primarily on the direction and strength of subpolar SW CRE changes and secondarily on the degree of strengthening negative SW CRE in the Arctic. Furthermore, even models with little change in subtropical and midlatitude SW CRE and compensating tropical SW CRE do not compensate fully for NH clear-sky albedo reductions between PI conditions and Mid.
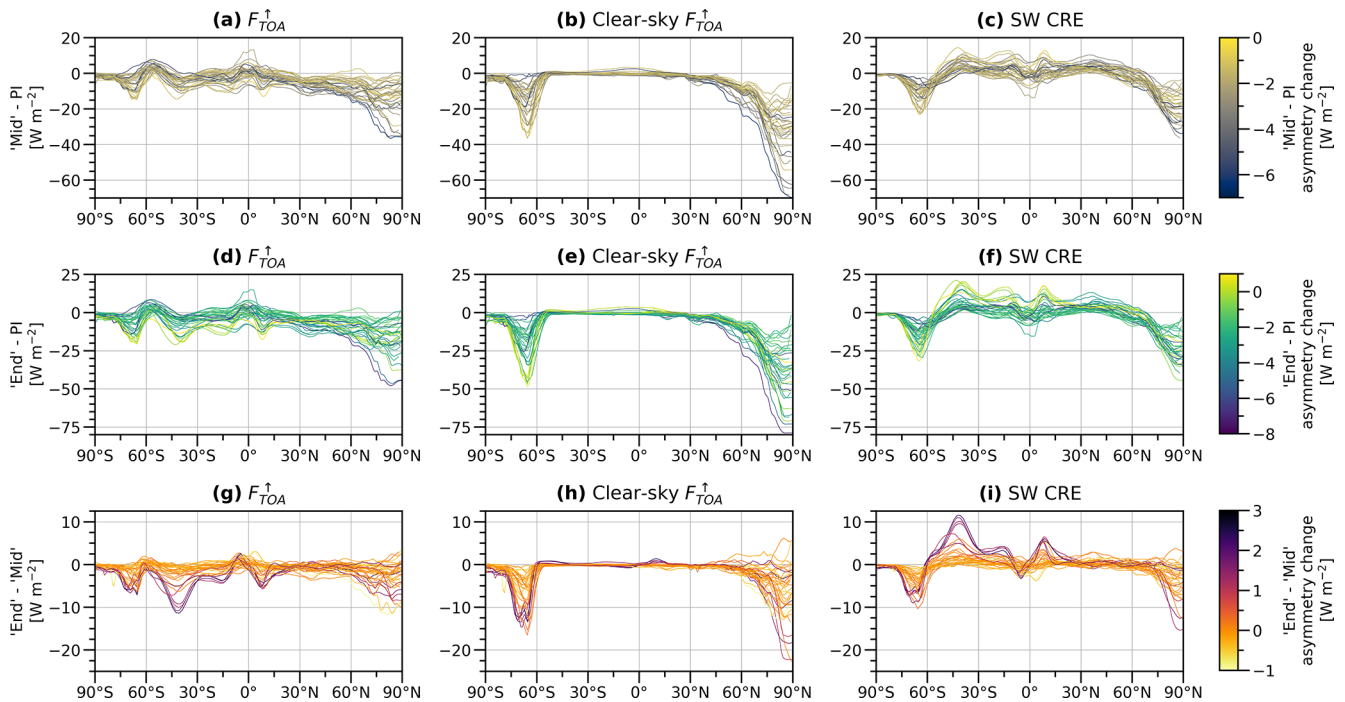
Figure 2. Meridional profiles of differences in zonal mean all- and clear-sky $F_{TOA}^{\uparrow}$, as well as SW CRE between **(a–c)** Mid and PI conditions, **(d–f)** End and PI conditions, and **(g–i)** End and Mid. Color scales represent the change in modeled mean hemispheric asymmetry between those periods.

3.3 Subsequent SH cloud responses to warming

One way to maintain a hemispheric albedo symmetry after perturbing the clear-sky hemispheric albedo difference would be that, when one hemisphere darkens, the other darkens as well. Models disagree on SH albedo reductions, which occur primarily in the SH extratropics, causing the divergence in modeled hemispheric albedo asymmetry after Mid noted in Sect. 3.1 and leading to some models recovering towards their PI mean albedo asymmetry; we will refer to compensations to the NH darkening offered by SH albedo reductions as *remote compensations*. In this section, we use modeled change in asymmetry between End and Mid as a measure of each model's remote compensation to the initial asymmetry response.

Comparing changes in SH midlatitude SW CRE against cloud properties (see Fig. S4) reveals that reductions in cloud fraction primarily drive weakening SW CRE ($R^2 = 0.95$), which out-compete increases in in-cloud cloud water content and changes in phase partitioning (greater fraction of liquid water content) that would otherwise make SW CRE more negative (Mülmenstädt et al., 2021) in some models. The reductions in SH midlatitude cloud cover reported here are also discussed by Gjermundsen et al. (2021), who investigated the differences in warming responses between two related models, CESM2 and NorESM2. These differences are attributed to the different ocean component models, in which Southern Ocean (SO) deep convection slowing occurs more quickly

in CESM2 than in NorESM2, allowing sea surface temperatures (SSTs) to increase more quickly and thus impact low cloud cover.

Beyond a divergence in SH extratropical SW CRE among models, we find a relationship between the evolution of climate and albedo at high latitudes in the SH with changes in SH extratropical cloud cover between Mid and End. Figure 4 shows changes in relevant SH polar climate variables plotted against changes in asymmetry between Mid and End. As the atmosphere warms (Fig. 4a), water vapor content increases in the SH (Fig. 4b), leading to greater poleward moisture transport and greater precipitation in the high SH latitudes. In the midlatitudes and sea ice zone ($\sim 50–75°$ S), this manifests increasingly as liquid precipitation, while snowfall is reduced; on the Antarctic continent, this mostly manifests as increased snowfall. SW CRE becomes more strongly negative over the Antarctic sea ice zone, which is to be expected as the contributions of the highly reflective ice-covered surface to albedo are reduced during warming.

Models disagree on whether poleward heat transport in the SH increases or decreases between Mid and End; however, models that lose more cloud cover in the SH midlatitudes exhibit only increasing poleward heat transport (see Fig. S5). Separating the MHT into its components shows that increased moist AHT due to increased poleward moisture transport (Fig. 4c) is the primary contributor to this strengthening poleward heat transport. Changes in tropospheric zonal
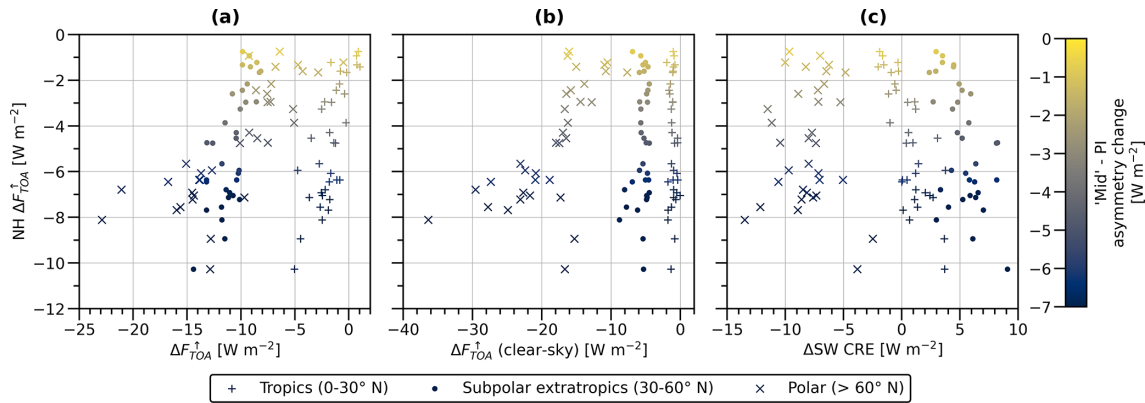
Figure 3. Area mean differences in **(a)** all-sky and **(b)** clear-sky $F_{TOA}^{\uparrow}$, as well as **(c)** SW CRE, in three ranges of latitudes plotted against the NH mean change in FTOA between Mid and PI conditions. The color scale is representative of the Mid minus PI albedo asymmetry difference.

and surface wind speeds (shown in Fig. S6) are indicative of a stronger poleward shift in the SH eddy-driven jet and the SH midlatitude storm track in models where SH extratropical cloud cover declines more strongly after the Mid period. It is also worth noting that models with greater SH extratropical cloud reductions agree on a southward shift of the ITCZ after the Mid period that occurs concurrently with SH cloud reductions (Fig. 2i), which is expected due to the increase in absorbed solar radiation in the SH extratropics changing the hemispheric difference in net radiative heating (Geng et al., 2022).

We find that models that lose more SH subpolar extratropical cloud cover have greater warming in the Antarctic and in the SH overall; these models also show greater reductions in Antarctic surface and planetary albedo and thus in albedo feedbacks. However, we find poor correlation between changes in SH sea ice extent and the evolution of asymmetry between Mid and End (shown in Fig. S7), indicating that the processes described here primarily affect Antarctic surface warming processes (i.e., the onset and strength of SH albedo feedback) in the amount of simulation time presented here.

Models with better representation of SH midlatitude clouds in PD conditions might also be expected to have better representations of their responses to forcing; to assess the remote compensations presented in this section, we compare model responses in models where cloud fraction and SW CRE are more similar to observations in the historical overlap period. We find that PI and PD mean cloud fraction and SW CRE are close among all models (linear regressions yield $R^2 > 0.99$ for both); therefore, we plot PD mean values of each against their responses to forcing in Fig. 5. The changes in SH extratropical cloud cover outlined in this section seem to have some dependency on the model state in an unforced climate. Models with the highest cloud fraction in this region see some of the greatest reductions in cloud fraction (Fig. 5a); however, the relation between mean-state SW

CRE and its response to forcing is inconsistent (Fig. 5b). This illustrates that it is difficult to judge whether remote compensations by SH extratropical clouds to a perturbation in hemispheric albedo asymmetry are likely or not, as a wide range of forced SW CRE responses in the SH extratropics is seen where PD mean cloud fraction and SW CRE are closest to observations (Fig. 5c). Thus, these measures are not enough to estimate which response in SH extratropical clouds is more realistic.

3.4 The relation between SW radiative feedback strength and the albedo symmetry

In the previous three sections, our results illustrate how responses in modeled hemispheric albedo asymmetries to CO_2 forcing differ and diverge due to varying cloud responses in both hemispheres. Here, we demonstrate how these cloud responses are related to the strength of SW cloud radiative feedbacks.

In Fig. 6a–b, we see that models that return to their preindustrial mean asymmetry through continued SH albedo reductions have stronger positive SW cloud radiative feedback strengths, associated with a stronger global mean decrease in albedo. Many models with negative or weakly positive SW cloud radiative feedback strengths remain within a 1 % difference in planetary albedo after warming through lower reductions in albedo in each hemisphere but tend to exhibit a stronger NH than SH albedo decrease. For comparison, the CERES EBAF standard deviation in the albedo asymmetry time series between 2000–2020 is 0.4 W m^{-2} ($\sim$ 0.1 %) (Jönsson and Bender, 2022), meaning that the perturbations in asymmetry due to strong forcing in all models 150 years after the onset of abrupt CO_2 forcing are an order of magnitude larger than those seen in the observational record.

To investigate the degree of cloud compensations to perturbations in the albedo asymmetries, we consider what must be true in order to maintain albedo symmetry ($\Delta\delta_{HD}\alpha \approx 0$)

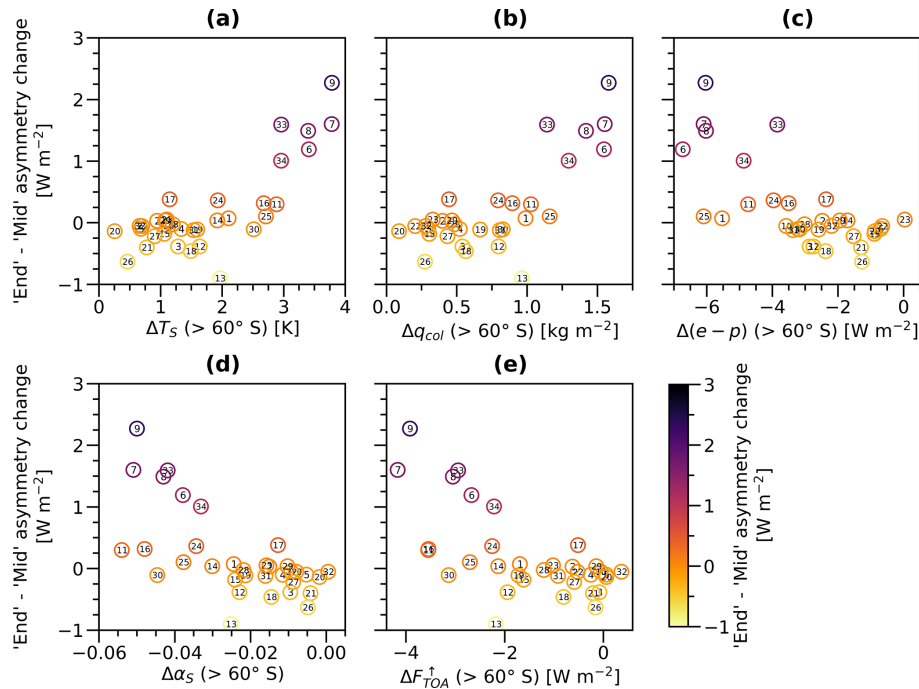**Figure 4.** Mean asymmetry changes plotted against SH polar (> 60° S)-area mean changes in **(a)** near-surface air temperature T_S, **(b)** vertically integrated atmospheric moisture content q_{col}, **(c)** evapotranspiration minus precipitation ($e − p$) expressed in energetic units, **(d)** surface albedo α_S, and **(d)** TOA upwelling SW radiation $F_{TOA}^{\uparrow}$ between Mid and End. Markers denote models as they are numbered in Table 1. The color scale depicts changes in asymmetry between End and Mid.
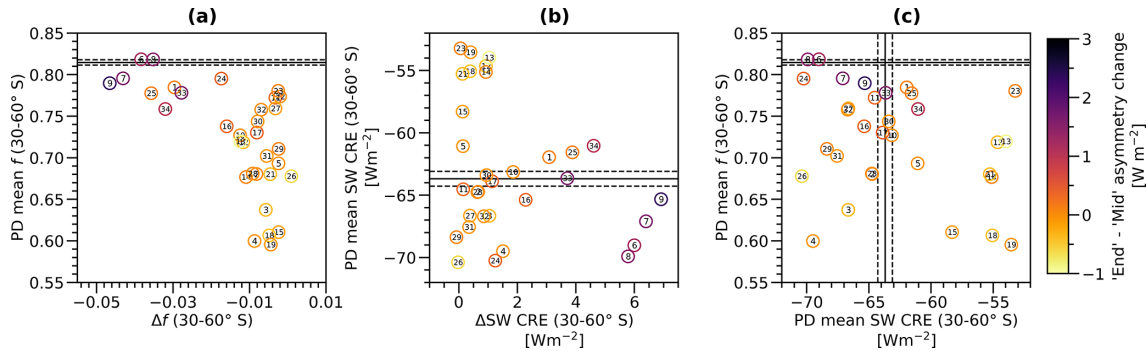
Figure 5. SH extratropical (30–60° S) mean **(a)** cloud fraction f and **(b)** SW CRE in PD conditions plotted against differences thereof between End and Mid. In **(c)**, PD mean SH extratropical f is plotted against PD mean SH extratropical SW CRE. Solid black lines represent CERES EBAF (SW CRE) and MODIS (cloud fraction) mean values over March 2000–February 2015, and dashed lines represent the bounds of 1 standard deviation in monthly mean anomalies. The color scale depicts modeled changes in asymmetry between End and Mid.

by expressing albedo in terms consistent with Eq. (1):

$$\Delta\delta_{HD}\alpha = \Delta\delta_{HD}\alpha^{CS} - \Delta\delta_{HD}\alpha^{CRE} \approx 0, \qquad (2)$$

that is, the clear-sky albedo asymmetry anomaly $\Delta\delta_{HD}\alpha^{CS}$ would have to be balanced by the changes in hemispheric differences in SW CRE ($\Delta\delta_{HD}\alpha^{CRE}$), i.e.,

$$\Delta\delta_{HD}\alpha^{CRE} \approx \Delta\delta_{HD}\alpha^{CS}. \qquad (3)$$

Figure 6c shows that models agree on changes in clear-sky albedo asymmetry between End and PI conditions. Here,

since models are unanimous in a negative clear-sky asymmetry response to warming due to the NH darkening, we consider only the cases where $\Delta\delta_{HD}\alpha^{CRE} > 0$ to be cases where clouds compensate for the clear-sky asymmetry anomaly. Figure 8d shows that this is usually not the case among models, and few models come close to the magnitude of $\Delta\delta_{HD}\alpha^{CRE}$ (~ 0.02) that would be needed in order for clouds to fully compensate for the clear-sky albedo asymmetry. The slope of the linear fit among model SW CRE responses lies close to 1, meaning that modeled SW CRE are nearly sym-
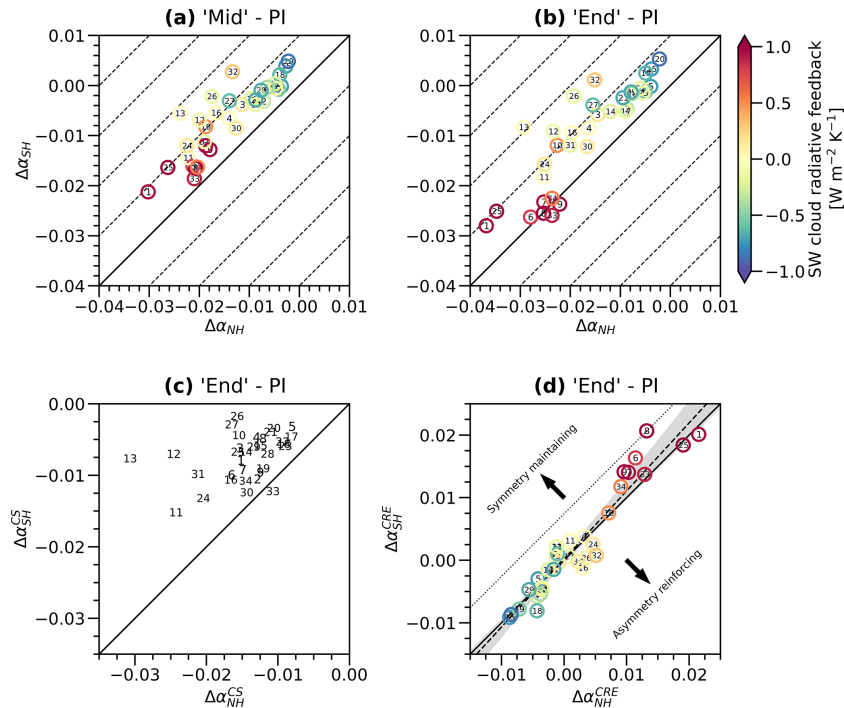
Figure 6. **(a, b)** Changes in the NH and SH hemispheric mean planetary albedo relative to their PI mean albedo ($\Delta\alpha_{NH}$ and $\Delta\alpha_{SH}$ respectively) plotted against each other on a "symmetry" phase space for all models in the **(a)** Mid and **(b)** End periods. The thick diagonal line represents symmetry scaled to PI conditions, while each dashed line parallel to this represents a 1 % hemispheric difference in albedo; models on the diagonal line remain close to their PI mean asymmetry. **(c, d)** Changes in NH and SH hemispheric mean **(c)** clear-sky albedo ($\Delta\alpha^{CS}$) and **(d)** SW CRE normalized by insolation ($\Delta\alpha^{CRE}$) between End and PI conditions. In **(d)**, the dotted line represents the multi-model mean clear-sky albedo asymmetry anomaly by the End period, and the dashed line depicts a linear regression among the models; shading represents the 95 % confidence interval for the slope. Estimates of model SW cloud radiative feedback strengths are given by the color of the marker. Markers denote models as they are numbered in Table 1.

metrical between hemispheres; a symmetric response lies within the 95 % confidence interval for the slope. That the intercept is near zero means that responses generally act in the same direction. However, that the slope could likely be greater than 1 reveals a tendency for models to have a greater SW CRE response in the SH than in the NH. This slope is in the direction that would be needed in order for clouds to compensate for the perturbation in clear-sky albedo asymmetry induced by warming but only in the case of more positive SW cloud radiative feedback.

Finally, the distribution of ECS among the models in relation to their responses in albedo asymmetry to CO_2 forcing is shown in Fig. 7. Responses in the asymmetry between PI conditions and End do not reveal a relation between the total asymmetry response to warming and ECS (Fig. 7a). However, the mechanism through which some models recover PI mean asymmetry – SH midlatitude cloud loss between Mid and End – contributes to positive SW cloud feedbacks. This seems to be consistent with those models also having amongst the highest ECS (Fig. 7b), although the relation is not strong ($R^2 = 0.30$ with $p = 0.002$).

4 Discussion

If a lasting hemispherically asymmetric albedo response to warming is possible, intermediate ranges of total SW radiative feedback strength estimates would be possible. However, if symmetry is to be maintained in a changing climate, hemispheric differences in surface albedo changes must be compensated for by clouds in one of two ways: by local or by remote compensation. With local compensation, surface albedo reductions are partially compensated for by cloud changes; such is the case, to some degree, in observed and modeled Arctic albedo responses to warming. With remote compensation, the requirement that albedo in both hemispheres declines symmetrically necessarily means that the global albedo reduction is greater. These two possibilities, local or remote compensations, would contribute negative or positive SW radiative feedbacks, respectively.

In the cases where clouds act in the direction of compensating for albedo asymmetry perturbations (Sect. 3.4, Fig. 6), there are no cases where NH local compensations – and thus negative SW cloud feedbacks – are strong enough for models to maintain their PI albedo asymmetry. Combinations where reductions in SW CRE are larger in the SH than in the NH –
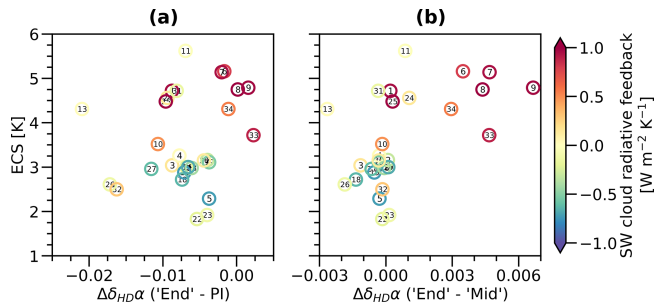
Figure 7. Estimates of ECS plotted against the **(a)** End minus PI and **(b)** End minus Mid albedo asymmetry anomaly $\Delta\delta_{HD}\alpha$. Estimates of model SW cloud radiative feedback strengths are given by the color of the marker. Markers denote models as they are numbered in Table 1.

and thus where SW cloud feedbacks are positive – do lead to instances where PI albedo asymmetries are maintained. This may mean that, if clouds do compensate for disturbances in the albedo asymmetry, an effective way for this to occur is via remote compensations, and scenarios involving more local compensations are unlikely to be capable of maintaining albedo symmetry. However, because of a lack of long-term measurements of Earth's radiative energy system with which to study the evolution of Earth's hemispheric albedo symmetry throughout changes in the climate and anthropogenic forcings, detecting the strength and causal sources of these compensations is currently challenging.

The fact that models with higher SH extratropical cloud fraction – and that are thereby in better agreement with observations – lose more clouds in response to warming could be taken as indication that a greater cloud loss and hence more positive cloud feedback and remote compensation are more realistic. On the other hand, the relation between unforced or historical mean SW CRE and the change in SW CRE in response to forcing is weak, leading to an inconsistent constraint on remote compensations. Models may also have realistic cloud properties in this region for the wrong reason, and models with more cloud cover may also see greater changes simply due to having more clouds in the unforced state to lose (Kajtar et al., 2021). The link between mean-state magnitude and forced response is ultimately not self-evident (McCoy et al., 2014; Zelinka et al., 2022; Kuma et al., 2023), and the timescales of the SH extratropical cloud changes involved may mean that albedo-symmetry-restoring remote compensations do not act on the time span of the observations that we presently have (Frey et al., 2017; Gjermundsen et al., 2021).

A remaining question is whether SH extratropical cloud reductions are to be seen in more models beyond the 150 years that are the required minimum simulation time for CMIP6 strong-forcing experiments. Gjermundsen et al. (2021) found that, despite NorESM2 having weaker SW cloud radiative feedbacks than CESM2 at year 150, the strength of these feedbacks is comparable after 500 years

of simulation when SO SSTs have risen to a similar degree. Previous results based on a single model show that SO deep convection also influences the occurrence of Antarctic warm events in a climate at equilibrium through processes similar to those presented in Sect. 3.3 (Pedro et al., 2016). It is possible that more models follow this pattern – and thereby exhibit remote compensations – on longer timescales. The sensitivity of modeled clouds to SSTs in this region would point to changes in SO SSTs being able to induce an SH albedo reduction and thus remote compensations. The overturning circulation that impacts SSTs in this region reaches between hemispheres and could thus present a cross-hemispheric communicator for energetic anomalies caused by changes in albedo.

Here, we have also shown that, in models, if a remote compensation to NH albedo reductions is accomplished by SH albedo reductions, the ITCZ will consequently move southward, in line with studies on changes in tropical precipitation under warming (e.g., Geng et al., 2022). If reductions in SH extratropical cloud cover and Antarctic albedo reinforce hemispheric differences in net radiative heating, a southward shift of the ITCZ may also occur and thus negate some of the remote compensation to asymmetry anomalies offered by SH extratropical albedo reductions, which may require more substantial extratropical albedo reductions to maintain hemispheric albedo symmetry. Although tropical clouds and albedo seem to play a secondary role in determining the observed hemispheric albedo symmetry on timescales longer than a year (Bender et al., 2017; Datseris and Stevens, 2021; Jönsson and Bender, 2022), this should also be taken into account in understanding hemispheric albedo-symmetry-maintaining mechanisms that involve the extratropics. However, model representations of tropical clouds, bias in the ITCZ position, and spurious, unrealistic ITCZ dynamics complicate projections of tropical clouds and albedo in a changing climate (e.g., Hwang and Frierson, 2013; Zhang et al., 2019a; Tian and Dong, 2020).

5   Conclusions

Following the observation that Earth's albedo is persistently hemispherically symmetric throughout the most recent 2 decades of satellite observations, we investigated responses in hemispheric differences in albedo to CO_2 forcing and their implications for cloud feedback, heat redistribution, and spatial patterns of warming. To do this, we made use of the evolution of hemispheric albedo differences in CMIP6 models when CO_2 concentrations are abruptly quadrupled.

In all models, NH albedo is immediately reduced due to albedo reductions in middle to high latitudes following ice loss and cloud changes, causing the hemispheric difference in albedo to be SH-favored relative to PI conditions consistently among all models. However, models do not agree on the strength of this initial response. In some models, cloud

cover increases in the NH to reduce the impact of clear-sky albedo reductions in the hemispheric mean, and in others, changes in NH cloud cover strengthens the all-sky albedo reductions. The former represents one way in which hemispheric albedo symmetry may be maintained: local compensations to albedo reductions.

Another possibility for maintaining hemispheric albedo symmetry involves remote compensations to hemispherically asymmetric albedo reductions: in some models, asymmetry states close to their PI conditions are restored when SH albedo is reduced, primarily via reductions in SH extratropical cloud cover. Here, we have shown that changes in SH extratropical cloud cover are linked with Antarctic polar amplification and changes in Antarctic albedo. When cloud cover is reduced in the SH extratropics, the increased absorbed energy is redistributed polewards, contributing to the spread in modeled Antarctic responses to CO_2 forcing.

These two pathways illustrate how mechanisms maintaining the hemispheric albedo symmetry impact the climate sensitivity through their implications for SW radiative feedbacks. Depending on the degree of local compensation (increasing total cloud contributions to albedo) and remote compensation (decreasing total cloud contributions to albedo), the implied SW cloud radiative feedback can be either negative or positive. Our results show that clouds may serve to suppress an asymmetric response in the hemispheric albedo difference to forcing so that the all-sky albedo is more hemispherically symmetric than clear-sky albedo, but they may not necessarily fully compensate for a perturbed hemispheric albedo difference. The lack of observational constraints or evidence for the existence of a symmetry-maintaining mechanism limits the possibility of evaluating model realism based on the model's degree of symmetry restoration. The lack of consistent pathways for symmetry restoration among the models limits the possibility of assessing a single mechanism for keeping the symmetry. However, there is clearly an implication for the strength of cloud–climate feedbacks depending on whether a possible mechanism that maintains the hemispheric albedo symmetry involves cross-hemispheric communication or not.

Appendix A

Table A1. Variables used in this study and their CMIP6 standard short names.

Variable	CMIP6 output variable name
Upwelling SW radiative flux at TOA (all-sky)	rsut
Upwelling SW radiative flux at TOA (clear-sky)	rsutcs
Incoming SW radiative flux at TOA	rsdt
Outgoing LW radiative flux at TOA	rlut
Net downward radiative flux at TOA	rtmt
Surface upwelling SW radiative flux	rsus
Surface downwelling SW radiative flux	rsds
Surface upwelling LW radiative flux	rlus
Surface downwelling LW radiative flux	rlds
Surface upward sensible heat flux	hfss
Surface upward latent heat flux	hfls
Cloud area fraction	clt
Vertically integrated atmospheric cloud condensed water content	clwvi
cloud condensed water content Vertically integrated cloud ice content	clivi
Vertically integrated atmospheric water vapor content	prw
Total precipitation	pr
Ice-phase precipitation	prsn
Total evapotranspiration and sublimation	evspsbl
Near-surface (10 m) wind speed	sfcWind
Eastward wind speed	ua
Sea ice area concentration	siconc

Table A2. Model output coverage in this study. Only variables where output was missing from some models are listed, and all other variables listed in Table A1 that are not present here are fully included in the study. Models where variable output was available for all experiments and presented in the study are marked with a plus sign (+), and a dash (−) is used where output from historical simulations was missing (only one variable, clt, from one model, GISS-E2-2-G).

Model		Variables included						
		clt	clwvi, clivi	prw	prsn	evspsbl	sfcWind	siconc
(1)	ACCESS-CM2	+		+	+	+	+	+
(2)	AWI-CM-1-1-MR	+	+	+	+	+	+	
(3)	BCC-CSM2-MR	+	+	+	+	+	+	
(4)	BCC-ESM1	+	+	+	+	+	+	
(5)	CAMS-CSM1-0	+	+	+		+	+	+
(6)	CESM2	+	+	+		+	+	+
(7)	CESM2-FV2	+		+	+	+	+	+
(8)	CESM2-WACCM	+	+	+		+	+	+
(9)	CESM2-WACCM-FV2	+		+	+	+	+	+
(10)	CMCC-CM2-SR5	+	+		+	+	+	+
(11)	CanESM5	+	+	+	+	+	+	+
(12)	EC-Earth3-AerChem	+		+	+	+		+
(13)	EC-Earth3-Veg	+		+	+			
(14)	FGOALS-f3-L	+	+		+	+	+	
(15)	FGOALS-g3	+		+	+	+	+	
(16)	GFDL-CM4	+	+	+	+	+	+	+
(17)	GFDL-ESM4	+	+	+	+	+	+	+
(18)	GISS-E2-1-G	+	+	+	+	+	+	
(19)	GISS-E2-1-H	+	+	+	+	+	+	+
(20)	GISS-E2-2-G	−		+	+	+	+	
(21)	IITM-ESM	+	+		+	+	+	+
(22)	INM-CM4-8	+	+	+	+	+	+	+
(23)	INM-CM5-0	+	+	+	+	+	+	+
(24)	IPSL-CM6A-LR	+	+	+	+	+	+	+
(25)	KACE-1-0-G	+	+	+	+	+	+	
(26)	MIROC6	+	+	+	+	+	+	+
(27)	MPI-ESM-1-2-HAM	+	+	+	+	+	+	+
(28)	MPI-ESM1-2-HR	+	+	+	+	+	+	+
(29)	MPI-ESM1-2-LR	+	+	+	+	+	+	+
(30)	MRI-ESM2-0	+	+	+	+	+	+	+
(31)	NESM3	+	+	+	+	+		+
(32)	NorESM2-MM	+	+	+	+	+	+	+
(33)	SAM0-UNICON	+	+	+	+	+	+	+
(34)	TaiESM1	+	+	+	+	+	+	

References

Bender, F. A.-M., Engström, A., Wood, R., and Charlson, R. J.: Evaluation of Hemispheric Asymmetries in Marine Cloud Radiative Properties, J. Climate, 30, 4131–4147, https://doi.org/10.1175/JCLI-D-16-0263.1, 2017.

Bentsen, M., Oliviè, D. J. L., Seland, y., Toniazzo, T., Gjermundsen, A., Graff, L. S., Debernard, J. B., Gupta, A. K., He, Y., Kirkevåg, A., Schwinger, J., Tjiputra, J., Aas, K. S., Bethke, I., Fan, Y., Griesfeller, J., Grini, A., Guo, C., Ilicak, M., Karset, I. H. H., Landgren, O. A., Liakka, J., Moseid, K. O., Nummelin, A., Spensberger, C., Tang, H., Zhang, Z., Heinze, C., Iversen, T., and Schulz, M.: NCC NorESM2-MM model output prepared for CMIP6 CMIP abrupt-4xCO2, Earth System Grid Federation, [data set], version 20191108, https://doi.org/10.22033/ESGF/CMIP6.7840, 2019a.

Bentsen, M., Oliviè, D. J. L., Seland, y., Toniazzo, T., Gjermundsen, A., Graff, L. S., Debernard, J. B., Gupta, A. K., He, Y., Kirkevåg, A., Schwinger, J., Tjiputra, J., Aas, K. S., Bethke, I., Fan, Y., Griesfeller, J., Grini, A., Guo, C., Ilicak, M., Karset, I. H. H., Landgren, O. A., Liakka, J., Moseid, K. O., Nummelin, A., Spensberger, C., Tang, H., Zhang, Z., Heinze, C., Iversen, T., and Schulz, M.: NCC NorESM2-MM model output prepared for CMIP6 CMIP piControl, Earth System Grid Federation, [data set], version 20191108, https://doi.org/10.22033/ESGF/CMIP6.8221, 2019b.

Bentsen, M., Oliviè, D. J. L., Seland, y., Toniazzo, T., Gjermundsen, A., Graff, L. S., Debernard, J. B., Gupta, A. K., He, Y., Kirkevåg, A., Schwinger, J., Tjiputra, J., Aas, K. S., Bethke, I., Fan, Y., Griesfeller, J., Grini, A., Guo, C., Ilicak, M., Karset, I. H. H., Landgren, O. A., Liakka, J., Moseid, K. O., Nummelin, A., Spensberger, C., Tang, H., Zhang, Z., Heinze, C., Iversen, T., and Schulz, M.: NCC NorESM2-MM model output prepared for CMIP6 CMIP historical, Earth System Grid Federation, [data set], version 20191108, https://doi.org/10.22033/ESGF/CMIP6.8040, 2019c.

Boucher, O., Denvil, S., Levavasseur, G., Cozic, A., Caubel, A., Foujols, M.-A., Meurdesoif, Y., Cadule, P., Devilliers, M., Ghattas, J., Lebas, N., Lurton, T., Mellul, L., Musat, I., Mignot, J., and Cheruy, F.: IPSL IPSL-CM6A-LR model output prepared for CMIP6 CMIP abrupt-4xCO2, Earth System Grid Federation, [data set], version 20190118, https://doi.org/10.22033/ESGF/CMIP6.5109, 2018a.

Boucher, O., Denvil, S., Levavasseur, G., Cozic, A., Caubel, A., Foujols, M.-A., Meurdesoif, Y., Cadule, P., Devilliers, M., Ghattas, J., Lebas, N., Lurton, T., Mellul, L., Musat, I., Mignot, J., and Cheruy, F.: IPSL IPSL-CM6A-LR model output prepared for CMIP6 CMIP historical, Earth System Grid Federation, [data set], version 20180803, https://doi.org/10.22033/ESGF/CMIP6.5195, 2018b.

Boucher, O., Denvil, S., Levavasseur, G., Cozic, A., Caubel, A., Foujols, M.-A., Meurdesoif, Y., Cadule, P., Devilliers, M., Ghattas, J., Lebas, N., Lurton, T., Mellul, L., Musat, I., Mignot, J., and Cheruy, F.: IPSL IPSL-CM6A-LR model output prepared for CMIP6 CMIP piControl,

Earth System Grid Federation, [data set], version 20200326, https://doi.org/10.22033/ESGF/CMIP6.5251, 2018c.

Byun, Y.-H., Lim, Y.-J., Sung, H. M., Kim, J., Sun, M., and Kim, B.-H.: NIMS-KMA KACE1.0-G model output prepared for CMIP6 CMIP abrupt-4xCO2, Earth System Grid Federation, [data set], version 20190916, https://doi.org/10.22033/ESGF/CMIP6.8348, 2019a.

Byun, Y.-H., Lim, Y.-J., Sung, H. M., Kim, J., Sun, M., and Kim, B.-H.: NIMS-KMA KACE1.0-G model output prepared for CMIP6 CMIP historical, Earth System Grid Federation, [data set], version 20190910, https://doi.org/10.22033/ESGF/CMIP6.8378, 2019b.

Byun, Y.-H., Lim, Y.-J., Sung, H. M., Kim, J., Sun, M., and Kim, B.-H.: NIMS-KMA KACE1.0-G model output prepared for CMIP6 CMIP piControl, Earth System Grid Federation, [data set], version 20191017, https://doi.org/10.22033/ESGF/CMIP6.8425, 2019c.

Cao, J. and Wang, B.: NUIST NESMv3 model output prepared for CMIP6 CMIP abrupt-4xCO2, Earth System Grid Federation, [data set], version 20190707, https://doi.org/10.22033/ESGF/CMIP6.8719, 2019a.

Cao, J. and Wang, B.: NUIST NESMv3 model output prepared for CMIP6 CMIP historical, Earth System Grid Federation,[data set], version 20190630, https://doi.org/10.22033/ESGF/CMIP6.8769, 2019b.

Cao, J. and Wang, B.: NUIST NESMv3 model output prepared for CMIP6 CMIP piControl, Earth System Grid Federation, [data set], version 20190708, https://doi.org/10.22033/ESGF/CMIP6.8776, 2019c.

Ceppi, P. and Hartmann, D. L.: Connections Between Clouds, Radiation, and Midlatitude Dynamics: a Review, Curr. Clim. Change Rep., 1, 94–102, https://doi.org/10.1007/s40641-015-0010-x, 2015.

Ceppi, P. and Nowack, P.: Observational evidence that cloud feedback amplifies global warming, P. Natl. Acad. Sci. USA, 118, e2026290118, https://doi.org/10.1073/pnas.2026290118, 2021.

Choudhury, A. D., Raghavan, K., Gopinathan, P. A., Narayanasetti, S., Singh, M., Panickal, S., and Modi, A.: CCCR-IITM IITM-ESM model output prepared for CMIP6 CMIP historical, Earth System Grid Federation, [data set], version 20191226, https://doi.org/10.22033/ESGF/CMIP6.3708, 2019.

Danabasoglu, G.: NCAR CESM2 model output prepared for CMIP6 CMIP abrupt-4xCO2, Earth System Grid Federation, [data set], version 20190927, https://doi.org/10.22033/ESGF/CMIP6.7519, 2019a.

Danabasoglu, G.: NCAR CESM2-WACCM model output prepared for CMIP6 CMIP abrupt-4xCO2, Earth System Grid Federation, [data set], version 20190425, https://doi.org/10.22033/ESGF/CMIP6.10039, 2019b.

Danabasoglu, G.: NCAR CESM2-FV2 model output prepared for CMIP6 CMIP historical, Earth System Grid Federation, [data set], version 20191120, https://doi.org/10.22033/ESGF/CMIP6.11297, 2019c.

Danabasoglu, G.: NCAR CESM2 model output prepared for CMIP6 CMIP historical, Earth System Grid Federation, [data set], version 20190308, https://doi.org/10.22033/ESGF/CMIP6.7627, 2019d.

Danabasoglu, G.: NCAR CESM2-WACCM-FV2 model output prepared for CMIP6 CMIP historical, Earth Sys-

tem Grid Federation, [data set], version 20191120, https://doi.org/10.22033/ESGF/CMIP6.11298, 2019e.

Danabasoglu, G.: NCAR CESM2-WACCM model output prepared for CMIP6 CMIP historical, Earth System Grid Federation, [data set], version 20190227, https://doi.org/10.22033/ESGF/CMIP6.10071, 2019f.

Danabasoglu, G.: NCAR CESM2-FV2 model output prepared for CMIP6 CMIP piControl, Earth System Grid Federation, [data set], version 20191120, https://doi.org/10.22033/ESGF/CMIP6.11301, 2019g.

Danabasoglu, G.: NCAR CESM2-WACCM model output prepared for CMIP6 CMIP piControl, Earth System Grid Federation, [data set], version 20190320, https://doi.org/10.22033/ESGF/CMIP6.10094, 2019h.

Danabasoglu, G.: NCAR CESM2-WACCM-FV2 model output prepared for CMIP6 CMIP piControl, Earth System Grid Federation, [data set], version 20191120, https://doi.org/10.22033/ESGF/CMIP6.11302, 2019i.

Danabasoglu, G.: NCAR CESM2-FV2 model output prepared for CMIP6 CMIP abrupt-4xCO2, Earth System Grid Federation, [data set], version 20200403, https://doi.org/10.22033/ESGF/CMIP6.11285, 2020a.

Danabasoglu, G.: NCAR CESM2-WACCM-FV2 model output prepared for CMIP6 CMIP abrupt-4xCO2, Earth System Grid Federation, [data set], version 20200403, https://doi.org/10.22033/ESGF/CMIP6.11286, 2020b.

Danabasoglu, G., Lawrence, D., Lindsay, K., Lipscomb, W., and Strand, G.: NCAR CESM2 model output prepared for CMIP6 CMIP piControl, Earth System Grid Federation, [data set], version 20190320, https://doi.org/10.22033/ESGF/CMIP6.7733, 2019.

Datseris, G. and Stevens, B.: Earth's Albedo and Its Symmetry, AGU Adv., 2, e2021AV000440, https://doi.org/10.1029/2021AV000440, 2021.

Diamond, M. S., Gristey, J. J., Kay, J. E., and Feingold, G.: Anthropogenic aerosol and cryosphere changes drive Earth's strong but transient clear-sky hemispheric albedo asymmetry, Commun. Earth Environ., 3, 206, https://doi.org/10.1038/s43247-022-00546-y, 2022.

Dix, M., Bi, D., Dobrohotoff, P., Fiedler, R., Harman, I., Law, R., Mackallah, C., Marsland, S., O'Farrell, S., Rashid, H., Srbinovsky, J., Sullivan, A., Trenham, C., Vohralik, P., Watterson, I., Williams, G., Woodhouse, M., Bodman, R., Dias, F. B., Domingues, C., Hannah, N., Heerdegen, A., Savita, A., Wales, S., Allen, C., Druken, K., Evans, B., Richards, C., Ridzwan, S. M., Roberts, D., Smillie, J., Snow, K., Ward, M., and Yang, R.: CSIRO-ARCCSS ACCESS-CM2 model output prepared for CMIP6 CMIP abrupt-4xCO2, Earth System Grid Federation, [data set], version 20191108, https://doi.org/10.22033/ESGF/CMIP6.4237, 2019a.

Dix, M., Bi, D., Dobrohotoff, P., Fiedler, R., Harman, I., Law, R., Mackallah, C., Marsland, S., O'Farrell, S., Rashid, H., Srbinovsky, J., Sullivan, A., Trenham, C., Vohralik, P., Watterson, I., Williams, G., Woodhouse, M., Bodman, R., Dias, F. B., Domingues, C., Hannah, N., Heerdegen, A., Savita, A., Wales, S., Allen, C., Druken, K., Evans, B., Richards, C., Ridzwan, S. M., Roberts, D., Smillie, J., Snow, K., Ward, M., and Yang, R.: CSIRO-ARCCSS ACCESS-CM2 model output prepared for CMIP6 CMIP piControl,

Earth System Grid Federation, [data set], version 20191112, https://doi.org/10.22033/ESGF/CMIP6.4311, 2019b.

Dix, M., Bi, D., Dobrohotoff, P., Fiedler, R., Harman, I., Law, R., Mackallah, C., Marsland, S., O'Farrell, S., Rashid, H., Srbinovsky, J., Sullivan, A., Trenham, C., Vohralik, P., Watterson, I., Williams, G., Woodhouse, M., Bodman, R., Dias, F. B., Domingues, C. M., Hannah, N., Heerdegen, A., Savita, A., Wales, S., Allen, C., Druken, K., Evans, B., Richards, C., Ridzwan, S. M., Roberts, D., Smillie, J., Snow, K., Ward, M., and Yang, R.: CSIRO-ARCCSS ACCESS-CM2 model output prepared for CMIP6 CMIP historical, Earth System Grid Federation, [data set], version 20191108, https://doi.org/10.22033/ESGF/CMIP6.4271, 2019c.

Donohoe, A., Armour, K. C., Roe, G. H., Battisti, D. S., and Hahn, L.: The Partitioning of Meridional Heat Transport from the Last Glacial Maximum to CO2 Quadrupling in Coupled Climate Models, J. Climate, 33, 4141–4165, https://doi.org/10.1175/JCLI-D-19-0797.1, 2020.

EC-Earth Consortium: EC-Earth-Consortium EC-Earth3-Veg model output prepared for CMIP6 CMIP abrupt-4xCO2, Earth System Grid Federation, [data set], version 20200225, https://doi.org/10.22033/ESGF/CMIP6.4524, 2019a.

EC-Earth Consortium: EC-Earth-Consortium EC-Earth3-Veg model output prepared for CMIP6 CMIP historical, Earth System Grid Federation, [data set], version 20200225, https://doi.org/10.22033/ESGF/CMIP6.4706, 2019b.

EC-Earth Consortium: EC-Earth-Consortium EC-Earth3-Veg model output prepared for CMIP6 CMIP piControl, Earth System Grid Federation, [data set], version 20200226, https://doi.org/10.22033/ESGF/CMIP6.4848,2019c.

EC-Earth Consortium: EC-Earth-Consortium EC-Earth3-AerChem model output prepared for CMIP6 CMIP abrupt-4xCO2, Earth System Grid Federation, [data set], version 20200622, https://doi.org/10.22033/ESGF/CMIP6.4519, 2020a.

EC-Earth Consortium: EC-Earth-Consortium EC-Earth3-AerChem model output prepared for CMIP6 CMIP historical, Earth System Grid Federation, [data set], version 20200624, https://doi.org/10.22033/ESGF/CMIP6.4701, 2020b.

EC-Earth Consortium: EC-Earth-Consortium EC-Earth3-AerChem model output prepared for CMIP6 CMIP piControl, Earth System Grid Federation, [data set], version 20200821, https://doi.org/10.22033/ESGF/CMIP6.4843, 2020c.

Eyring, V., Bony, S., Meehl, G. A., Senior, C. A., Stevens, B., Stouffer, R. J., and Taylor, K. E.: Overview of the Coupled Model Intercomparison Project Phase 6 (CMIP6) experimental design and organization, Geosci. Model Dev., 9, 1937–1958, https://doi.org/10.5194/gmd-9-1937-2016, 2016.

Forster, P., Storelvmo, T., Armour, K., Collins, W., Dufresne, J. L., Frame, D., Lunt, D. J., Mauritsen, T., Palmer, M. D., Watanabe, M., Wild, M., and Zhang, H.: The Earth's Energy Budget, Climate Feedbacks, and Climate Sensitivity, in: Climate Change 2021: The Physical Science Basis. Contribution of Working Group I to the Sixth Assessment Report of the Intergovernmental Panel on Climate Change, edited by: Masson-Delmotte, V., Zhai, P., Pirani, A., Connors, S. L., Péan, C., Berger, S., Caud, N., Chen, Y., Goldfarb, L., Gomis, M. I., Huang, M., Leitzell, K., Lonnoy, E., Matthews, J. B. R., Maycock, T. K., Waterfield, T., Yelekçi, O., Yu, R., and Zhou, B., book section 7, Cambridge University Press, Cam-

bridge, United Kingdom and New York, NY, USA, 923–1054, https://doi.org/:10.1017/9781009157896.009, 2021.

Frey, W. R., Maroon, E. A., Pendergrass, A. G., and Kay, J. E.: Do Southern Ocean Cloud Feedbacks Matter for 21st Century Warming?, Geophys. Res. Lett., 44, 12447–12456, https://doi.org/10.1002/2017GL076339, 2017.

Geng, Y.-F., Xie, S.-P., Zheng, X.-T., Long, S.-M., Kang, S. M., Lin, X., and Song, Z.-H.: CMIP6 Intermodel Spread in Interhemispheric Asymmetry of Tropical Climate Response to Greenhouse Warming: Extratropical Ocean Effects, J. Climate, 35, 4869–4882, https://doi.org/10.1175/JCLI-D-21-0541.1, 2022.

Gettelman, A., Bardeen, C. G., McCluskey, C. S., Järvinen, E., Stith, J., Bretherton, C., McFarquhar, G., Twohy, C., D'Alessandro, J., and Wu, W.: Simulating Observations of Southern Ocean Clouds and Implications for Climate, J. Geophys. Res.-Atmos., 125, e2020JD032619, https://doi.org/10.1029/2020JD032619, 2020.

Gjermundsen, A., Nummelin, A., Olivié, D., Bentsen, M., Seland, Ø., and Schulz, M.: Shutdown of Southern Ocean convection controls long-term greenhouse gas-induced warming, Nat. Geosci., 14, 724–731, https://doi.org/10.1038/s41561-021-00825-x, 2021.

Gopinathan, P. A., Narayanasetti, S., Choudhury, A. D., Singh, M., Raghavan, K., Panickal, S., and Modi, A.: CCCR-IITM IITM-ESM model output prepared for CMIP6 CMIP abrupt-4xCO2, Earth System Grid Federation, [data set], version 20191223, https://doi.org/10.22033/ESGF/CMIP6.3516, 2019.

Gregory, J. M., Ingram, W. J., Palmer, M. A., Jones, G. S., Stott, P. A., Thorpe, R. B., Lowe, J. A., Johns, T. C., and Williams, K. D.: A new method for diagnosing radiative forcing and climate sensitivity, Geophys. Res. Lett., 31, L03205, https://doi.org/10.1029/2003GL018747, 2004.

Guo, H., John, J. G., Blanton, C., McHugh, C., Nikonov, S., Radhakrishnan, A., Rand, K., Zadeh, N. T., Balaji, V., Durachta, J., Dupuis, C., Menzel, R., Robinson, T., Underwood, S., Vahlenkamp, H., Bushuk, M., Dunne, K. A., Dussin, R., Gauthier, P. P., Ginoux, P., Griffies, S. M., Hallberg, R., Harrison, M., Hurlin, W., Lin, P., Malyshev, S., Naik, V., Paulot, F., Paynter, D. J., Ploshay, J., Reichl, B. G., Schwarzkopf, D. M., Seman, C. J., Shao, A., Silvers, L., Wyman, B., Yan, X., Zeng, Y., Adcroft, A., Dunne, J. P., Held, I. M., Krasting, J. P., Horowitz, L. W., Milly, P., Shevliakova, E., Winton, M., Zhao, M., and Zhang, R.: NOAA-GFDL GFDL-CM4 model output abrupt-4xCO2, Earth System Grid Federation, [data set], version 20180701, https://doi.org/10.22033/ESGF/CMIP6.8486, 2018a.

Guo, H., John, J. G., Blanton, C., McHugh, C., Nikonov, S., Radhakrishnan, A., Rand, K., Zadeh, N. T., Balaji, V., Durachta, J., Dupuis, C., Menzel, R., Robinson, T., Underwood, S., Vahlenkamp, H., Bushuk, M., Dunne, K. A., Dussin, R., Gauthier, P. P., Ginoux, P., Griffies, S. M., Hallberg, R., Harrison, M., Hurlin, W., Lin, P., Malyshev, S., Naik, V., Paulot, F., Paynter, D. J., Ploshay, J., Reichl, B. G., Schwarzkopf, D. M., Seman, C. J., Shao, A., Silvers, L., Wyman, B., Yan, X., Zeng, Y., Adcroft, A., Dunne, J. P., Held, I. M., Krasting, J. P., Horowitz, L. W., Milly, P., Shevliakova, E., Winton, M., Zhao, M., and Zhang, R.: NOAA-GFDL GFDL-CM4 model output piControl, Earth System Grid Federation, [data set], version 20180701, https://doi.org/10.22033/ESGF/CMIP6.8666, 2018b.

Guo, H., John, J. G., Blanton, C., McHugh, C., Nikonov, S., Radhakrishnan, A., Rand, K., Zadeh, N. T., Balaji, V., Durachta, J., Dupuis, C., Menzel, R., Robinson, T., Underwood, S., Vahlenkamp, H., Bushuk, M., Dunne, K. A., Dussin, R., Gauthier, P. P., Ginoux, P., Griffies, S. M., Hallberg, R., Harrison, M., Hurlin, W., Lin, P., Malyshev, S., Naik, V., Paulot, F., Paynter, D. J., Ploshay, J., Reichl, B. G., Schwarzkopf, D. M., Seman, C. J., Shao, A., Silvers, L., Wyman, B., Yan, X., Zeng, Y., Adcroft, A., Dunne, J. P., Held, I. M., Krasting, J. P., Horowitz, L. W., Milly, P., Shevliakova, E., Winton, M., Zhao, M., and Zhang, R.: NOAA-GFDL GFDL-CM4 model output historical, Earth System Grid Federation, version 20180701, https://doi.org/10.22033/ESGF/CMIP6.8594, 2018c.

Hahn, L. C., Armour, K. C., Zelinka, M. D., Bitz, C. M., and Donohoe, A.: Contributions to Polar Amplification in CMIP5 and CMIP6 Models, Front. Earth Sci., 9, 710036, https://doi.org/10.3389/feart.2021.710036, 2021.

Hwang, Y.-T. and Frierson, D. M. W.: Link between the double-Intertropical Convergence Zone problem and cloud biases over the Southern Ocean, P. Natl. Acad. Sci. USA, 110, 4935–4940, https://doi.org/10.1073/pnas.1213302110, 2013.

Jungclaus, J., Bittner, M., Wieners, K.-H., Wachsmann, F., Schupfner, M., Legutke, S., Giorgetta, M., Reick, C., Gayler, V., Haak, H., de Vrese, P., Raddatz, T., Esch, M., Mauritsen, T., von Storch, J.-S., Behrens, J., Brovkin, V., Claussen, M., Crueger, T., Fast, I., Fiedler, S., Hagemann, S., Hohenegger, C., Jahns, T., Kloster, S., Kinne, S., Lasslop, G., Kornblueh, L., Marotzke, J., Matei, D., Meraner, K., Mikolajewicz, U., Modali, K., Müller, W., Nabel, J., Notz, D., Peters-von Gehlen, K., Pincus, R., Pohlmann, H., Pongratz, J., Rast, S., Schmidt, H., Schnur, R., Schulzweida, U., Six, K., Stevens, B., Voigt, A., and Roeckner, E.: MPI-M MPI-ESM1.2-HR model output prepared for CMIP6 CMIP abrupt-4xCO2, Earth System Grid Federation, [data set], version 20190710, https://doi.org/10.22033/ESGF/CMIP6.6458, 2019a.

Jungclaus, J., Bittner, M., Wieners, K.-H., Wachsmann, F., Schupfner, M., Legutke, S., Giorgetta, M., Reick, C., Gayler, V., Haak, H., de Vrese, P., Raddatz, T., Esch, M., Mauritsen, T., von Storch, J.-S., Behrens, J., Brovkin, V., Claussen, M., Crueger, T., Fast, I., Fiedler, S., Hagemann, S., Hohenegger, C., Jahns, T., Kloster, S., Kinne, S., Lasslop, G., Kornblueh, L., Marotzke, J., Matei, D., Meraner, K., Mikolajewicz, U., Modali, K., Müller, W., Nabel, J., Notz, D., Peters-von Gehlen, K., Pincus, R., Pohlmann, H., Pongratz, J., Rast, S., Schmidt, H., Schnur, R., Schulzweida, U., Six, K., Stevens, B., Voigt, A., and Roeckner, E.: MPI-M MPI-ESM1.2-HR model output prepared for CMIP6 CMIP piControl, Earth System Grid Federation, [data set], version 20190710, https://doi.org/10.22033/ESGF/CMIP6.6674, 2019b.

Jungclaus, J., Bittner, M., Wieners, K.-H., Wachsmann, F., Schupfner, M., Legutke, S., Giorgetta, M., Reick, C., Gayler, V., Haak, H., de Vrese, P., Raddatz, T., Esch, M., Mauritsen, T., von Storch, J.-S., Behrens, J., Brovkin, V., Claussen, M., Crueger, T., Fast, I., Fiedler, S., Hagemann, S., Hohenegger, C., Jahns, T., Kloster, S., Kinne, S., Lasslop, G., Kornblueh, L., Marotzke, J., Matei, D., Meraner, K., Mikolajewicz, U., Modali, K., Müller, W., Nabel, J., Notz, D., Peters-von Gehlen, K., Pincus, R., Pohlmann, H., Pongratz, J., Rast, S., Schmidt, H., Schnur, R., Schulzweida, U., Six, K., Stevens, B., Voigt, A., and Roeckner,

E.: MPI-M MPI-ESM1.2-HR model output prepared for CMIP6 CMIP historical, Earth System Grid Federation, [data set], version 20190710, https://doi.org/10.22033/ESGF/CMIP6.6594, 2019c.

Jönsson, A. and Bender, F. A.-M.: Persistence and Variability of Earth's Interhemispheric Albedo Symmetry in 19 Years of CERES EBAF Observations, J. Climate, 35, 249–268, https://doi.org/10.1175/JCLI-D-20-0970.1, 2022.

Kajtar, J. B., Santoso, A., Collins, M., Taschetto, A. S., England, M. H., and Frankcombe, L. M.: CMIP5 Intermodel Relationships in the Baseline Southern Ocean Climate System and With Future Projections, Earth's Future, 9, e2020EF001873, https://doi.org/10.1029/2020EF001873, 2021.

Krasting, J. P., John, J. G., Blanton, C., McHugh, C., Nikonov, S., Radhakrishnan, A., Rand, K., Zadeh, N. T., Balaji, V., Durachta, J., Dupuis, C., Menzel, R., Robinson, T., Underwood, S., Vahlenkamp, H., Dunne, K. A., Gauthier, P. P., Ginoux, P., Griffies, S. M., Hallberg, R., Harrison, M., Hurlin, W., Malyshev, S., Naik, V., Paulot, F., Paynter, D. J., Ploshay, J., Reichl, B. G., Schwarzkopf, D. M., Seman, C. J., Silvers, L., Wyman, B., Zeng, Y., Adcroft, A., Dunne, J. P., Dussin, R., Guo, H., He, J., Held, I. M., Horowitz, L. W., Lin, P., Milly, P., Shevliakova, E., Stock, C., Winton, M., Wittenberg, A. T., Xie, Y., and Zhao, M.: NOAA-GFDL GFDL-ESM4 model output prepared for CMIP6 CMIP abrupt-4xCO2, Earth System Grid Federation, [data set], version 20180701, https://doi.org/10.22033/ESGF/CMIP6.8489, 2018a.

Krasting, J. P., John, J. G., Blanton, C., McHugh, C., Nikonov, S., Radhakrishnan, A., Rand, K., Zadeh, N. T., Balaji, V., Durachta, J., Dupuis, C., Menzel, R., Robinson, T., Underwood, S., Vahlenkamp, H., Dunne, K. A., Gauthier, P. P., Ginoux, P., Griffies, S. M., Hallberg, R., Harrison, M., Hurlin, W., Malyshev, S., Naik, V., Paulot, F., Paynter, D. J., Ploshay, J., Reichl, B. G., Schwarzkopf, D. M., Seman, C. J., Silvers, L., Wyman, B., Zeng, Y., Adcroft, A., Dunne, J. P., Dussin, R., Guo, H., He, J., Held, I. M., Horowitz, L. W., Lin, P., Milly, P., Shevliakova, E., Stock, C., Winton, M., Wittenberg, A. T., Xie, Y., and Zhao, M.: NOAA-GFDL GFDL-ESM4 model output prepared for CMIP6 CMIP piControl, Earth System Grid Federation, [data set], version 20180701, https://doi.org/10.22033/ESGF/CMIP6.8669, 2018b.

Krasting, J. P., John, J. G., Blanton, C., McHugh, C., Nikonov, S., Radhakrishnan, A., Rand, K., Zadeh, N. T., Balaji, V., Durachta, J., Dupuis, C., Menzel, R., Robinson, T., Underwood, S., Vahlenkamp, H., Dunne, K. A., Gauthier, P. P., Ginoux, P., Griffies, S. M., Hallberg, R., Harrison, M., Hurlin, W., Malyshev, S., Naik, V., Paulot, F., Paynter, D. J., Ploshay, J., Reichl, B. G., Schwarzkopf, D. M., Seman, C. J., Silvers, L., Wyman, B., Zeng, Y., Adcroft, A., Dunne, J. P., Dussin, R., Guo, H., He, J., Held, I. M., Horowitz, L. W., Lin, P., Milly, P., Shevliakova, E., Stock, C., Winton, M., Wittenberg, A. T., Xie, Y., and Zhao, M.: NOAA-GFDL GFDL-ESM4 model output prepared for CMIP6 CMIP historical, Earth System Grid Federation, [data set], version 20190726, https://doi.org/10.22033/ESGF/CMIP6.8597, 2018c.

Kuma, P., Bender, F. A.-M., Schuddeboom, A., McDonald, A. J., and Seland, Ø.: Machine learning of cloud types in satellite observations and climate models, Atmos. Chem. Phys., 23, 523–549, https://doi.org/10.5194/acp-23-523-2023, 2023.

Lee, W.-L. and Liang, H.-C.: AS-RCEC TaiESM1.0 model output prepared for CMIP6 CMIP abrupt-4xCO2, Earth

System Grid Federation, [data set], version 20200310, https://doi.org/10.22033/ESGF/CMIP6.9709, 2020a.

Lee, W.-L. and Liang, H.-C.: AS-RCEC TaiESM1.0 model output prepared for CMIP6 CMIP historical, Earth System Grid Federation, [data set], version 20200623, https://doi.org/10.22033/ESGF/CMIP6.9755, 2020b.

Lee, W.-L. and Liang, H.-C.: AS-RCEC TaiESM1.0 model output prepared for CMIP6 CMIP piControl, Earth System Grid Federation, [data set], version 20200211, https://doi.org/10.22033/ESGF/CMIP6.9798, 2020c.

Li, L.: CAS FGOALS-g3 model output prepared for CMIP6 CMIP abrupt-4xCO2, Earth System Grid Federation, [data set], version 20191230, https://doi.org/10.22033/ESGF/CMIP6.3177, 2019a.

Li, L.: CAS FGOALS-g3 model output prepared for CMIP6 CMIP historical, Earth System Grid Federation, [data set], version 20190818, https://doi.org/10.22033/ESGF/CMIP6.3356, 2019b.

Li, L.: CAS FGOALS-g3 model output prepared for CMIP6 CMIP piControl, Earth System Grid Federation, [data set], version 20190818, https://doi.org/10.22033/ESGF/CMIP6.3448, 2019c.

Loeb, N. G., Doelling, D. R., Wang, H., Su, W., Nguyen, C., Corbett, J. G., Liang, L., Mitrescu, C., Rose, F. G., and Kato, S.: Clouds and the Earth's Radiant Energy System (CERES) Energy Balanced and Filled (EBAF) Top-of-Atmosphere (TOA) Edition-4.0 Data Product, J. Climate, 31, 895–918, https://doi.org/10.1175/JCLI-D-17-0208.1, 2018.

Lovato, T. and Peano, D.: CMCC CMCC-CM2-SR5 model output prepared for CMIP6 CMIP abrupt-4xCO2, Earth System Grid Federation, [data set], version 20200616, https://doi.org/10.22033/ESGF/CMIP6.3731, 2020a.

Lovato, T. and Peano, D.: CMCC CMCC-CM2-SR5 model output prepared for CMIP6 CMIP historical, Earth System Grid Federation, [data set], version 20200616, https://doi.org/10.22033/ESGF/CMIP6.3825, 2020b.

Lovato, T. and Peano, D.: CMCC CMCC-CM2-SR5 model output prepared for CMIP6 CMIP piControl, Earth System Grid Federation, [data set], version 20200616, https://doi.org/10.22033/ESGF/CMIP6.3874, 2020c.

McCoy, D. T., Hartmann, D. L., and Grosvenor, D. P.: Observed Southern Ocean Cloud Properties and Shortwave Reflection, Part II: Phase Changes and Low Cloud Feedback, J. Climate, 27, 8858–8868, https://doi.org/10.1175/JCLI-D-14-00288.1, 2014.

Meehl, G. A., Senior, C. A., Eyring, V., Flato, G., Lamarque, J.-F., Stouffer, R. J., Taylor, K. E., and Schlund, M.: Context for interpreting equilibrium climate sensitivity and transient climate response from the CMIP6 Earth system models, Sci. Adv., 6, eaba1981, https://doi.org/10.1126/sciadv.aba1981, 2020.

Mülmenstädt, J., Salzmann, M., Kay, J. E., Zelinka, M. D., Ma, P.-L., Nam, C., Kretzschmar, J., Hörnig, S., and Quaas, J.: An underestimated negative cloud feedback from cloud lifetime changes, Nat. Clim. Change, 11, 508–513, https://doi.org/10.1038/s41558-021-01038-1, 2021.

Myhre, G., Boucher, O., Bréon, F.-M., Forster, P., and Shindell, D.: Declining uncertainty in transient climate response as CO2 forcing dominates future climate change, Nat. Geosci., 8, 181–185, https://doi.org/10.1038/ngeo2371, 2015.

Narayanasetti, S., Panickal, S., Raghavan, K., Gopinathan, P. A., Choudhury, A. D., and Singh, M.: CCCR-IITM IITM-ESM model output prepared for CMIP6 CMIP piControl,

Earth System Grid Federation, [data set], version 20191120, https://doi.org/10.22033/ESGF/CMIP6.3710, 2019.

NASA Goddard Institute for Space Studies: NASA-GISS GISS-E2.1G model output prepared for CMIP6 CMIP abrupt-4xCO2, Earth System Grid Federation, [data set], version 20181002, https://doi.org/10.22033/ESGF/CMIP6.6976, 2018a.

NASA Goddard Institute for Space Studies: NASA-GISS GISS-E2.1G model output prepared for CMIP6 CMIP historical, Earth System Grid Federation, [data set], version 20180827, https://doi.org/10.22033/ESGF/CMIP6.7127, 2018b.

NASA Goddard Institute for Space Studies: NASA-GISS GISS-E2.1G model output prepared for CMIP6 CMIP piControl, Earth System Grid Federation, [data set], version 20180824, https://doi.org/10.22033/ESGF/CMIP6.7380, 2018c.

NASA Goddard Institute for Space Studies: NASA-GISS GISS-E2.1H model output prepared for CMIP6 CMIP piControl, Earth System Grid Federation, version 20190410, https://doi.org/10.22033/ESGF/CMIP6.7381, 2018d.

NASA Goddard Institute for Space Studies: NASA-GISS GISS-E2.1H model output prepared for CMIP6 CMIP abrupt-4xCO2, Earth System Grid Federation, [data set], version 20190403, https://doi.org/10.22033/ESGF/CMIP6.6977, 2019a.

NASA Goddard Institute for Space Studies: NASA-GISS GISS-E2.1H model output prepared for CMIP6 CMIP historical, Earth System Grid Federation, [data set], version 20190403, https://doi.org/10.22033/ESGF/CMIP6.7128, 2019b.

NASA Goddard Institute for Space Studies: NASA-GISS GISS-E2-2-G model output prepared for CMIP6 CMIP abrupt-4xCO2, Earth System Grid Federation, [data set], version 20191120, https://doi.org/10.22033/ESGF/CMIP6.6978, 2019c.

NASA Goddard Institute for Space Studies: NASA-GISS GISS-E2-2-G model output prepared for CMIP6 CMIP piControl, Earth System Grid Federation, [data set], version 20191120, https://doi.org/10.22033/ESGF/CMIP6.7382, 2019d.

NASA/LARC/SD/ASDC: CERES Energy Balanced and Filled (EBAF) TOA and Surface Monthly means data in netCDF Edition 4.1 [data set], NASA Langley Atmospheric Science Data Center DAAC, [data set], https://doi.org/10.5067/TERRA-AQUA/CERES/EBAF_L3B.004.1 (last access: 28 October 2022), 2019.

Neubauer, D., Ferrachat, S., Siegenthaler-Le Drian, C., Stoll, J., Folini, D. S., Tegen, I., Wieners, K.-H., Mauritsen, T., Stemmler, I., Barthel, S., Bey, I., Daskalakis, N., Heinold, B., Kokkola, H., Partridge, D., Rast, S., Schmidt, H., Schutgens, N., Stanelle, T., Stier, P., Watson-Parris, D., and Lohmann, U.: HAMMOZ-Consortium MPI-ESM1.2-HAM model output prepared for CMIP6 CMIP abrupt-4xCO2, Earth System Grid Federation, [data set], version 20190629, https://doi.org/10.22033/ESGF/CMIP6.5000, 2019a.

Neubauer, D., Ferrachat, S., Siegenthaler-Le Drian, C., Stoll, J., Folini, D. S., Tegen, I., Wieners, K.-H., Mauritsen, T., Stemmler, I., Barthel, S., Bey, I., Daskalakis, N., Heinold, B., Kokkola, H., Partridge, D., Rast, S., Schmidt, H., Schutgens, N., Stanelle, T., Stier, P., Watson-Parris, D., and Lohmann, U.: HAMMOZ-Consortium MPI-ESM1.2-HAM model output prepared for CMIP6 CMIP piControl, Earth System Grid Federation, [data set], version 20200120, https://doi.org/10.22033/ESGF/CMIP6.5037, 2019b.

Neubauer, D., Ferrachat, S., Siegenthaler-Le Drian, C., Stoll, J., Folini, D. S., Tegen, I., Wieners, K.-H., Mauritsen, T., Stemmler, I., Barthel, S., Bey, I., Daskalakis, N., Heinold, B., Kokkola, H., Partridge, D., Rast, S., Schmidt, H., Schutgens, N., Stanelle, T., Stier, P., Watson-Parris, D., and Lohmann, U.: HAMMOZ-Consortium MPI-ESM1.2-HAM model output prepared for CMIP6 CMIP historical, Earth System Grid Federation, [data set], version 20190627, https://doi.org/10.22033/ESGF/CMIP6.5016, 2019c.

Park, S. and Shin, J.: SNU SAM0-UNICON model output prepared for CMIP6 CMIP abrupt-4xCO2, Earth System Grid Federation, [data set], version 20190323, https://doi.org/10.22033/ESGF/CMIP6.7783, 2019a.

Park, S. and Shin, J.: SNU SAM0-UNICON model output prepared for CMIP6 CMIP historical, Earth System Grid Federation, [data set], version 20190323, https://doi.org/10.22033/ESGF/CMIP6.7789, 2019b.

Park, S. and Shin, J.: SNU SAM0-UNICON model output prepared for CMIP6 CMIP piControl, Earth System Grid Federation, [data set], version 20190910, https://doi.org/10.22033/ESGF/CMIP6.7791, 2019c.

Pedro, J. B., Martin, T., Steig, E. J., Jochum, M., Park, W., and Rasmussen, S. O.: Southern Ocean deep convection as a driver of Antarctic warming events, Geophys. Res. Lett., 43, 2192–2199, https://doi.org/10.1002/2016GL067861, 2016.

Rong, X.: CAMS CAMS_CSM1.0 model output prepared for CMIP6 CMIP abrupt-4xCO2, Earth System Grid Federation, [data set], version 20190708, https://doi.org/10.22033/ESGF/CMIP6.9708, 2019a.

Rong, X.: CAMS CAMS_CSM1.0 model output prepared for CMIP6 CMIP historical, Earth System Grid Federation, [data set], version 20190708, https://doi.org/10.22033/ESGF/CMIP6.9754, 2019b.

Rong, X.: CAMS CAMS_CSM1.0 model output prepared for CMIP6 CMIP piControl, Earth System Grid Federation, [data set], version 20190729, https://doi.org/10.22033/ESGF/CMIP6.9797, 2019c.

Rugenstein, M. and Hakuba, M.: Connecting hemispheric asymmetries of planetary albedo and surface temperature, Geophys. Res. Lett., https://doi.org/10.1029/2022GL101802, accepted, 2023.

Rugenstein, M., Bloch-Johnson, J., Gregory, J., Andrews, T., Mauritsen, T., Li, C., Frölicher, T. L., Paynter, D., Danabasoglu, G., Yang, S., Dufresne, J.-L., Cao, L., Schmidt, G. A., Abe-Ouchi, A., Geoffroy, O., and Knutti, R.: Equilibrium Climate Sensitivity Estimated by Equilibrating Climate Models, Geophys. Res. Lett., 47, e2019GL083898, https://doi.org/10.1029/2019GL083898, 2020.

Semmler, T., Danilov, S., Rackow, T., Sidorenko, D., Barbi, D., Hegewald, J., Sein, D., Wang, Q., and Jung, T.: AWI AWI-CM1.1MR model output prepared for CMIP6 CMIP abrupt-4xCO2, Earth System Grid Federation, [data set], version 20191108, https://doi.org/10.22033/ESGF/CMIP6.2568, 2018a.

Semmler, T., Danilov, S., Rackow, T., Sidorenko, D., Barbi, D., Hegewald, J., Sein, D., Wang, Q., and Jung, T.: AWI AWI-CM1.1MR model output prepared for CMIP6 CMIP historical, Earth System Grid Federation, [data set], version 20200511, https://doi.org/10.22033/ESGF/CMIP6.2686, 2018b.

Semmler, T., Danilov, S., Rackow, T., Sidorenko, D., Barbi, D., Hegewald, J., Sein, D., Wang, Q., and Jung, T.: AWI AWI-CM1.1MR model output prepared for CMIP6 CMIP piControl, Earth System Grid Federation, [data set], version 20191015, https://doi.org/10.22033/ESGF/CMIP6.2777, 2018c.

Sledd, A. and L'Ecuyer, T. S.: A Cloudier Picture of Ice-Albedo Feedback in CMIP6 Models, Front. Earth Sci., 9, 769844, https://doi.org/10.3389/feart.2021.769844, 2021.

Stephens, G. L., O'Brien, D., Webster, P. J., Pilewski, P., Kato, S., and Li, J.-L.: The albedo of Earth, Rev. Geophys., 53, 141–163, https://doi.org/10.1002/2014RG000449, 2015.

Stephens, G. L., Hakuba, M. Z., Kato, S., Gettleman, A., Dufresne, J.-L., Andrews, T., Cole, J. N. S., Willem, U., and Mauritsen, T.: The changing nature of Earth's reflected sunlight, P. Roy. Soc. A-Math. Phy., 478, 20220053, https://doi.org/10.1098/rspa.2022.0053, 2022.

Stevens, B. and Schwartz, S. E.: Observing and Modeling Earth's Energy Flows, Surv. Geophys., 33, 779–816, https://doi.org/10.1007/s10712-012-9184-0, 2012.

Swart, N. C., Cole, J. N., Kharin, V. V., Lazare, M., Scinocca, J. F., Gillett, N. P., Anstey, J., Arora, V., Christian, J. R., Jiao, Y., Lee, W. G., Majaess, F., Saenko, O. A., Seiler, C., Seinen, C., Shao, A., Solheim, L., von Salzen, K., Yang, D., Winter, B., and Sigmond, M.: CCCma CanESM5 model output prepared for CMIP6 CMIP abrupt-4xCO2, Earth System Grid Federation, [data set], version 20190429, https://doi.org/10.22033/ESGF/CMIP6.3532, 2019a.

Swart, N. C., Cole, J. N., Kharin, V. V., Lazare, M., Scinocca, J. F., Gillett, N. P., Anstey, J., Arora, V., Christian, J. R., Jiao, Y., Lee, W. G., Majaess, F., Saenko, O. A., Seiler, C., Seinen, C., Shao, A., Solheim, L., von Salzen, K., Yang, D., Winter, B., and Sigmond, M.: CCCma CanESM5 model output prepared for CMIP6 CMIP piControl, Earth System Grid Federation, [data set], version 20190429, https://doi.org/10.22033/ESGF/CMIP6.3673, 2019b.

Swart, N. C., Cole, J. N., Kharin, V. V., Lazare, M., Scinocca, J. F., Gillett, N. P., Anstey, J., Arora, V., Christian, J. R., Jiao, Y., Lee, W. G., Majaess, F., Saenko, O. A., Seiler, C., Seinen, C., Shao, A., Solheim, L., von Salzen, K., Yang, D., Winter, B., and Sigmond, M.: CCCma CanESM5 model output prepared for CMIP6 CMIP historical, Earth System Grid Federation, [data set], version 20190429, https://doi.org/10.22033/ESGF/CMIP6.3610, 2019c.

Szopa, S., Naik, V., Adhikary, B., Artaxo, P., Berntsen, T., Collins, W. D., Fuzzi, S., Gallardo, L., Kiendler Scharr, A., Klimont, Z., Liao, H., Unger, N., and Zanis, P.: Short-Lived Climate Forcers, in: Climate Change 2021: The Physical Science Basis. Contribution of Working Group I to the Sixth Assessment Report of the Intergovernmental Panel on Climate Change, edited by: Masson-Delmotte, V., Zhai, P., Pirani, A., Connors, S. L., Péan, C., Berger, S., Caud, N., Chen, Y., Goldfarb, L., Gomis, M. I., Huang, M., Leitzell, K., Lonnoy, E., Matthews, J. B. R., Maycock, T. K., Waterfield, T., Yelekçi, O., Yu, R., and Zhou, B., book section 6, Cambridge University Press, Cambridge, United Kingdom and New York, NY, USA, 817–922, https://doi.org/10.1017/9781009157896.008, 2021.

Tatebe, H. and Watanabe, M.: MIROC MIROC6 model output prepared for CMIP6 CMIP abrupt-4xCO2, Earth System Grid Federation, [data set], version 20190705, https://doi.org/10.22033/ESGF/CMIP6.5411, 2018a.

Tatebe, H. and Watanabe, M.: MIROC MIROC6 model output prepared for CMIP6 CMIP historical, Earth System Grid Federation, [data set], version 20190311, https://doi.org/10.22033/ESGF/CMIP6.5603, 2018b.

Tatebe, H. and Watanabe, M.: MIROC MIROC6 model output prepared for CMIP6 CMIP piControl, Earth System Grid Federation, [data set], version 20190311, https://doi.org/10.22033/ESGF/CMIP6.5711, 2018c.

Tian, B. and Dong, X.: The Double-ITCZ Bias in CMIP3, CMIP5, and CMIP6 Models Based on Annual Mean Precipitation, Geophys. Res. Lett., 47, e2020GL087232, https://doi.org/10.1029/2020GL087232, 2020.

Voigt, A., Stevens, B., Bader, J., and Mauritsen, T.: The Observed Hemispheric Symmetry in Reflected Shortwave Irradiance, J. Climate, 26, 468–477, 2013.

Voigt, A., Stevens, B., Bader, J., and Mauritsen, T.: Compensation of Hemispheric Albedo Asymmetries by Shifts of the ITCZ and Tropical Clouds, J. Climate, 27, 1029–1045, https://doi.org/10.1175/JCLI-D-13-00205.1, 2014.

Volodin, E., Mortikov, E., Gritsun, A., Lykossov, V., Galin, V., Diansky, N., Gusev, A., Kostrykin, S., Iakovlev, N., Shestakova, A., and Emelina, S.: INM INM-CM4-8 model output prepared for CMIP6 CMIP abrupt-4xCO2, Earth System Grid Federation, [data set], version 20190529, https://doi.org/10.22033/ESGF/CMIP6.4931, 2019a.

Volodin, E., Mortikov, E., Gritsun, A., Lykossov, V., Galin, V., Diansky, N., Gusev, A., Kostrykin, S., Iakovlev, N., Shestakova, A., and Emelina, S.: INM INM-CM4-8 model output prepared for CMIP6 CMIP historical, Earth System Grid Federation, [data set], version 20190530, https://doi.org/10.22033/ESGF/CMIP6.5069, 2019b.

Volodin, E., Mortikov, E., Gritsun, A., Lykossov, V., Galin, V., Diansky, N., Gusev, A., Kostrykin, S., Iakovlev, N., Shestakova, A., and Emelina, S.: INM INM-CM4-8 model output prepared for CMIP6 CMIP piControl, Earth System Grid Federation, [data set], version 20190605, https://doi.org/10.22033/ESGF/CMIP6.5080, 2019c.

Volodin, E., Mortikov, E., Gritsun, A., Lykossov, V., Galin, V., Diansky, N., Gusev, A., Kostrykin, S., Iakovlev, N., Shestakova, A., and Emelina, S.: INM INM-CM5-0 model output prepared for CMIP6 CMIP abrupt-4xCO2, Earth System Grid Federation, [data set], version 20190610, https://doi.org/10.22033/ESGF/CMIP6.4932, 2019d.

Volodin, E., Mortikov, E., Gritsun, A., Lykossov, V., Galin, V., Diansky, N., Gusev, A., Kostrykin, S., Iakovlev, N., Shestakova, A., and Emelina, S.: INM INM-CM5-0 model output prepared for CMIP6 CMIP historical, Earth System Grid Federation, [data set], version 20190610, https://doi.org/10.22033/ESGF/CMIP6.5070, 2019e.

Volodin, E., Mortikov, E., Gritsun, A., Lykossov, V., Galin, V., Diansky, N., Gusev, A., Kostrykin, S., Iakovlev, N., Shestakova, A., and Emelina, S.: INM INM-CM5-0 model output prepared for CMIP6 CMIP piControl, Earth System Grid Federation, [data set], version 20190619, https://doi.org/10.22033/ESGF/CMIP6.5081, 2019f.

Vonder Haar, T. H. and Suomi, V. E.: Measurements of the Earth's Radiation Budget from Satellites During a Five-Year Period, Part I: Extended Time and Space Means,

J. Atmos. Sci., 28, 305–314, https://doi.org/10.1175/1520-0469(1971)028<0305:MOTERB>2.0.CO;2, 1971.

Wieners, K.-H., Giorgetta, M., Jungclaus, J., Reick, C., Esch, M., Bittner, M., Legutke, S., Schupfner, M., Wachsmann, F., Gayler, V., Haak, H., de Vrese, P., Raddatz, T., Mauritsen, T., von Storch, J.-S., Behrens, J., Brovkin, V., Claussen, M., Crueger, T., Fast, I., Fiedler, S., Hagemann, S., Hohenegger, C., Jahns, T., Kloster, S., Kinne, S., Lasslop, G., Kornblueh, L., Marotzke, J., Matei, D., Meraner, K., Mikolajewicz, U., Modali, K., Müller, W., Nabel, J., Notz, D., Peters-von Gehlen, K., Pincus, R., Pohlmann, H., Pongratz, J., Rast, S., Schmidt, H., Schnur, R., Schulzweida, U., Six, K., Stevens, B., Voigt, A., and Roeckner, E.: MPI-M MPI-ESM1.2-LR model output prepared for CMIP6 CMIP abrupt-4xCO2, Earth System Grid Federation, [data set], version 20190710, https://doi.org/10.22033/ESGF/CMIP6.6459, 2019a.

Wieners, K.-H., Giorgetta, M., Jungclaus, J., Reick, C., Esch, M., Bittner, M., Legutke, S., Schupfner, M., Wachsmann, F., Gayler, V., Haak, H., de Vrese, P., Raddatz, T., Mauritsen, T., von Storch, J.-S., Behrens, J., Brovkin, V., Claussen, M., Crueger, T., Fast, I., Fiedler, S., Hagemann, S., Hohenegger, C., Jahns, T., Kloster, S., Kinne, S., Lasslop, G., Kornblueh, L., Marotzke, J., Matei, D., Meraner, K., Mikolajewicz, U., Modali, K., Müller, W., Nabel, J., Notz, D., Peters-von Gehlen, K., Pincus, R., Pohlmann, H., Pongratz, J., Rast, S., Schmidt, H., Schnur, R., Schulzweida, U., Six, K., Stevens, B., Voigt, A., and Roeckner, E.: MPI-M MPI-ESM1.2-LR model output prepared for CMIP6 CMIP piControl, Earth System Grid Federation, [data set], version 20190710, https://doi.org/10.22033/ESGF/CMIP6.6675, 2019b.

Wieners, K.-H., Giorgetta, M., Jungclaus, J., Reick, C., Esch, M., Bittner, M., Legutke, S., Schupfner, M., Wachsmann, F., Gayler, V., Haak, H., de Vrese, P., Raddatz, T., Mauritsen, T., von Storch, J.-S., Behrens, J., Brovkin, V., Claussen, M., Crueger, T., Fast, I., Fiedler, S., Hagemann, S., Hohenegger, C., Jahns, T., Kloster, S., Kinne, S., Lasslop, G., Kornblueh, L., Marotzke, J., Matei, D., Meraner, K., Mikolajewicz, U., Modali, K., Müller, W., Nabel, J., Notz, D., Peters-von Gehlen, K., Pincus, R., Pohlmann, H., Pongratz, J., Rast, S., Schmidt, H., Schnur, R., Schulzweida, U., Six, K., Stevens, B., Voigt, A., and Roeckner, E.: MPI-M MPI-ESM1.2-LR model output prepared for CMIP6 CMIP historical, Earth System Grid Federation, [data set], version 20190710, https://doi.org/10.22033/ESGF/CMIP6.6595, 2019c.

Wu, T., Chu, M., Dong, M., Fang, Y., Jie, W., Li, J., Li, W., Liu, Q., Shi, X., Xin, X., Yan, J., Zhang, F., Zhang, J., Zhang, L., and Zhang, Y.: BCC BCC-CSM2MR model output prepared for CMIP6 CMIP abrupt-4xCO2, Earth System Grid Federation, [data set], version 20181016, https://doi.org/10.22033/ESGF/CMIP6.2845, 2018a.

Wu, T., Chu, M., Dong, M., Fang, Y., Jie, W., Li, J., Li, W., Liu, Q., Shi, X., Xin, X., Yan, J., Zhang, F., Zhang, J., Zhang, L., and Zhang, Y.: BCC BCC-CSM2MR model output prepared for CMIP6 CMIP historical, Earth System Grid Federation, [data set], version 20181126, https://doi.org/10.22033/ESGF/CMIP6.2948, 2018b.

Wu, T., Chu, M., Dong, M., Fang, Y., Jie, W., Li, J., Li, W., Liu, Q., Shi, X., Xin, X., Yan, J., Zhang, F., Zhang, J., Zhang, L., and Zhang, Y.: BCC BCC-CSM2MR model output prepared for CMIP6 CMIP esm-piControl, Earth System Grid Federation, [data set], version 20181016, https://doi.org/10.22033/ESGF/CMIP6.2907, 2018c.

Yu, Y.: CAS FGOALS-f3-L model output prepared for CMIP6 CMIP abrupt-4xCO2, Earth System Grid Federation, [data set], version 20191018 https://doi.org/10.22033/ESGF/CMIP6.3176,, 2019a.

Yu, Y.: CAS FGOALS-f3-L model output prepared for CMIP6 CMIP historical, Earth System Grid Federation, [data set], version 20190927, https://doi.org/10.22033/ESGF/CMIP6.3355, 2019b.

Yu, Y.: CAS FGOALS-f3-L model output prepared for CMIP6 CMIP piControl, Earth System Grid Federation, [data set], version 20191029, https://doi.org/10.22033/ESGF/CMIP6.3447, 2019c.

Yukimoto, S., Koshiro, T., Kawai, H., Oshima, N., Yoshida, K., Urakawa, S., Tsujino, H., Deushi, M., Tanaka, T., Hosaka, M., Yoshimura, H., Shindo, E., Mizuta, R., Ishii, M., Obata, A., and Adachi, Y.: MRI MRI-ESM2.0 model output prepared for CMIP6 CMIP historical, Earth System Grid Federation, [data set], version 20190222, https://doi.org/10.22033/ESGF/CMIP6.6842, 2019a.

Yukimoto, S., Koshiro, T., Kawai, H., Oshima, N., Yoshida, K., Urakawa, S., Tsujino, H., Deushi, M., Tanaka, T., Hosaka, M., Yoshimura, H., Shindo, E., Mizuta, R., Ishii, M., Obata, A., and Adachi, Y.: MRI MRI-ESM2.0 model output prepared for CMIP6 CMIP abrupt-4xCO2, Earth System Grid Federation, [data set], version 20190308, https://doi.org/10.22033/ESGF/CMIP6.6755, 2019b.

Yukimoto, S., Koshiro, T., Kawai, H., Oshima, N., Yoshida, K., Urakawa, S., Tsujino, H., Deushi, M., Tanaka, T., Hosaka, M., Yoshimura, H., Shindo, E., Mizuta, R., Ishii, M., Obata, A., and Adachi, Y.: MRI MRI-ESM2.0 model output prepared for CMIP6 CMIP piControl, Earth System Grid Federation, [data set], version 20190222, https://doi.org/10.22033/ESGF/CMIP6.6900, 2019c.

Zelinka, M. D., Myers, T. A., McCoy, D. T., Po-Chedley, S., Caldwell, P. M., Ceppi, P., Klein, S. A., and Taylor, K. E.: Causes of Higher Climate Sensitivity in CMIP6 Models, Geophys. Res. Lett., 47, e2019GL085782, https://doi.org/10.1029/2019GL085782, 2020.

Zelinka, M. D., Klein, S. A., Qin, Y., and Myers, T. A.: Evaluating Climate Models' Cloud Feedbacks Against Expert Judgment, J. Geophys. Res.-Atmos., 127, e2021JD035198, https://doi.org/10.1029/2021JD035198, 2022.

Zhang, G. J., Song, X., and Wang, Y.: The double ITCZ syndrome in GCMs: A coupled feedback problem among convection, clouds, atmospheric and ocean circulations, Atmos. Res., 229, 255–268, https://doi.org/10.1016/j.atmosres.2019.06.023, 2019a.

Zhang, J., Wu, T., Shi, X., Zhang, F., Li, J., Chu, M., Liu, Q., Yan, J., Ma, Q., and Wei, M.: BCC BCC-ESM1 model output prepared for CMIP6 CMIP historical, Earth System Grid Federation, [data set], version 20181214, https://doi.org/10.22033/ESGF/CMIP6.2949, 2018a.

Zhang, J., Wu, T., Shi, X., Zhang, F., Li, J., Chu, M., Liu, Q., Yan, J., Ma, Q., and Wei, M.: BCC BCC-ESM1 model output prepared for CMIP6 CMIP piControl, Earth System Grid Federation, [data set], version 20181214, https://doi.org/10.22033/ESGF/CMIP6.3017, 2018b.

Zhang, J., Wu, T., Shi, X., Zhang, F., Li, J., Chu, M., Liu, Q., Yan, J., Ma, Q., and Wei, M.: BCC BCC-ESM1 model output prepared for CMIP6 CMIP abrupt-4xCO2, Earth System Grid Federation, [data set], version 20190613, https://doi.org/10.22033/ESGF/CMIP6.2846, 2019b.